Title

Imaging shapes of atomic nuclei in high-energy nuclear collisions.

Journal

Nature: New biology, 635(8037)

Publication Date

2024-11-01

DOI

10.1038/s41586-024-08097-2

Peer reviewed

Article

Imaging shapes of atomic nuclei in high-energy nuclear collisions

https://doi.org/10.1038/s41586-024-08097-2

Received: 11 January 2024

Accepted: 23 September 2024

Published online: 6 November 2024

Open access

Check for updates

STAR Collaboration*✉

Atomic nuclei are self-organized, many-body quantum systems bound by strong nuclear forces within femtometre-scale space. These complex systems manifest a variety of shapes[1–3], traditionally explored using non-invasive spectroscopic techniques at low energies[4,5]. However, at these energies, their instantaneous shapes are obscured by long-timescale quantum fluctuations, making direct observation challenging. Here we introduce the collective-flow-assisted nuclear shape-imaging method, which images the nuclear global shape by colliding them at ultrarelativistic speeds and analysing the collective response of outgoing debris. This technique captures a collision-specific snapshot of the spatial matter distribution within the nuclei, which, through the hydrodynamic expansion, imprints patterns on the particle momentum distribution observed in detectors[6,7]. We benchmark this method in collisions of ground-state uranium-238 nuclei, known for their elongated, axial-symmetric shape. Our findings show a large deformation with a slight deviation from axial symmetry in the nuclear ground state, aligning broadly with previous low-energy experiments. This approach offers a new method for imaging nuclear shapes, enhances our understanding of the initial conditions in high-energy collisions and addresses the important issue of nuclear structure evolution across energy scales.

More than 99.9% of the visible matter in the cosmos resides in the centre of atoms—the atomic nuclei composed of nucleons (protons and neutrons). Our knowledge of their global structure primarily comes from spectroscopic or scattering experiments[4,5,8] at beam energies below hundreds of MeV per nucleon. These studies show that most nuclei are ellipsoidally deformed, with greater deformation in nuclei distant from magic numbers[9] (2, 8, 20, 28, 50, 82 and 126). Investigating nuclear shape across the Segrè chart has been an important area of research over many decades and is crucial for topics such as nucleosynthesis[10], nuclear fission[11] and neutrinoless double beta decay ($0\nu\beta\beta$) (ref. 12).

In a collective model picture, the ellipsoidal shape of a nucleus with mass number A is defined in the intrinsic (body-fixed) frame, in which its surface $R(\theta, \phi)$ is described by[1,3]

$$R(\theta,\phi) = R_0(1+\beta_2[\cos\gamma Y_{2,0} + \sin\gamma Y_{2,2}]). \quad (1)$$

Here $R_0 \approx 1.2A^{1/3}$ fm represents the nuclear radius. The spherical harmonics in the real basis $Y_{l,m}(\theta, \phi)$, the quadrupole deformation magnitude β_2 and the triaxiality parameter γ define the nuclear shape. The γ parameter, spanning 0°–60°, controls the ratios of principal radii. Specifically, $\gamma = 0°$ corresponds to a prolate shape, $\gamma = 60°$ an oblate shape, and values in between $0° < \gamma < 60°$ to a triaxial shape. Although most nuclei are axially symmetric (prolate or oblate) or have a fluctuating γ value (γ-soft), the rigid triaxial shape is uncommon[13]. An example of an axial-symmetric, prolate-deformed nucleus is shown in Fig. 1a.

Nuclear shapes, even in ground states, are not fixed. They exhibit zero-point quantum fluctuations involving various collective and nucleonic degrees of freedom (DOF) at different timescales. These fluctuations superimpose on each other in the laboratory frame. In well-deformed nuclei such as ^{238}U, dominant fluctuations are in the rotational DOF with a timescale of $\tau_{\rm rot} \sim I/\hbar \sim 10^3$–$10^4$ fm/c (1 fm/c = 3 × 10^{-24} s = 3 yoctoseconds)[14], where I denotes the moment of inertia (Fig. 1b). Consequently, measurement processes in spectroscopic methods, lasting orders of magnitude longer than $\tau_{\rm rot}$, capture a coherent superposition of wavefunctions in all orientations. Their shapes are usually inferred by comparing spectroscopic data (Fig. 1c) with model calculations[15,16]. Traditional electron–nucleus scattering experiments, although faster than $\tau_{\rm rot}$, probe mainly localized regions of the nucleus, giving an orientation-averaged spherical image after accumulating many events, in which the impact of deformation manifests as a broadening of the charge distribution[1,3,8].

New shape-imaging method

To directly observe the global shape of the nuclei, a measurement must (1) be much quicker than $\tau_{\rm rot}$ and (2) provide access to the many-body nucleon distribution in each nucleus. High-energy nuclear collisions, an utterly destructive process, remarkably fulfil these criteria. Conducted at the Relativistic Heavy-Ion Collider (RHIC) and the Large Hadron Collider (LHC) with centre-of-mass energies per nucleon pair ($\sqrt{s_{\rm NN}}$) reaching up to 5,000 GeV, these collisions completely obliterate the nuclei, temporarily forming a quark–gluon plasma (QGP)—a hot, dense matter of interacting quarks and gluons[6,7]. The nuclear shape influences the geometry of QGP and its collective expansion, imprinting itself on the momentum distribution of the produced particles. In an ironic twist, this effectively realizes Richard Feynman's analogy of the

*A list of authors and their affiliations appears at the end of the paper. ✉e-mail: star-publication@bnl.gov

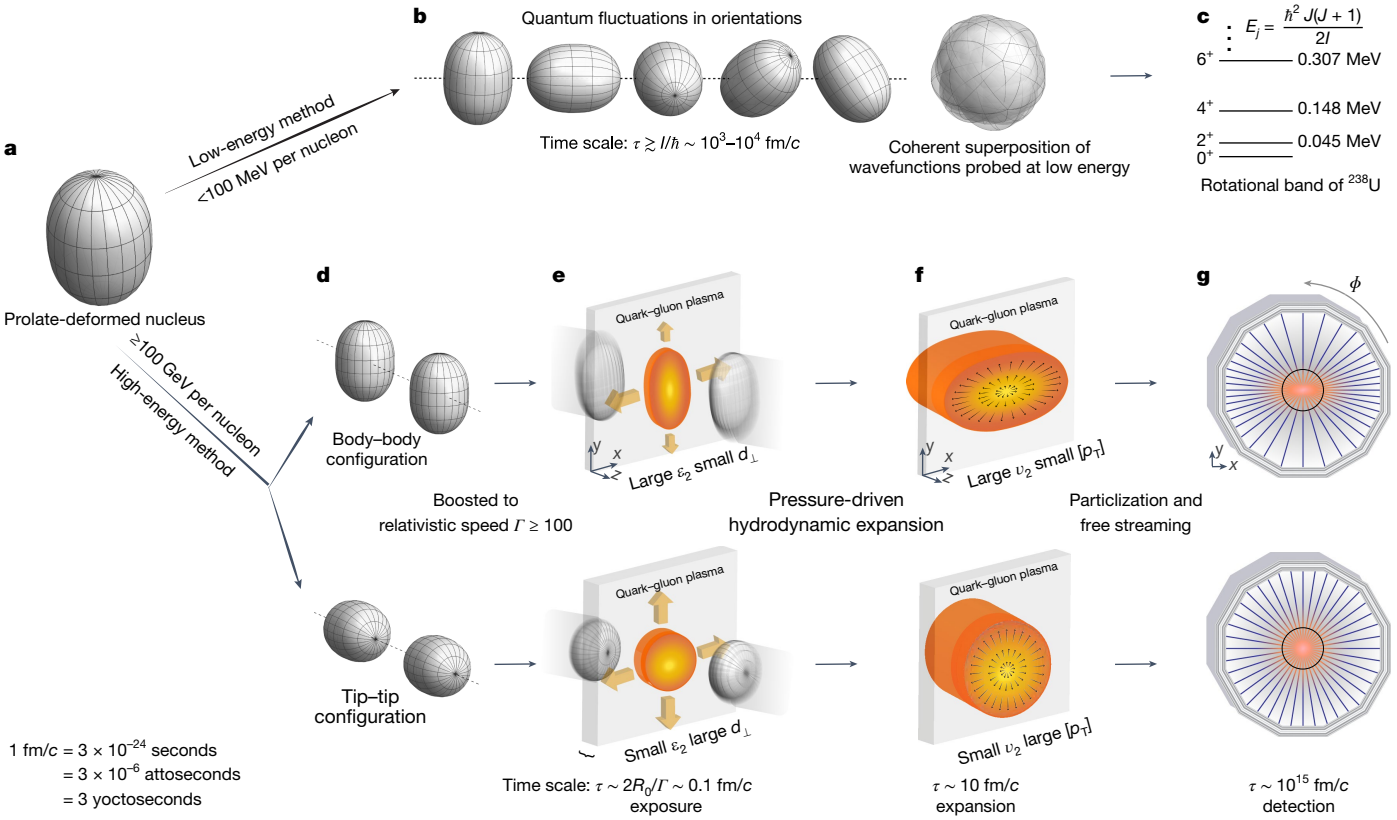

Fig. 1 | Methods for determining the nuclear shape in low and high energies. **a**, Cartoon of a well-deformed prolate-shaped nucleus. **b**, Quantum fluctuations over Euler angles for this nucleus and associated overall timescale. **c**, Quantum mechanical manifestation of the deformation in terms of the first rotational band of ^{238}U. **d**, Aligning the two nuclei in the head-on body–body configuration (top) and tip–tip configuration (bottom). **e**, High-energy collision of two Lorentz-contracted nuclei and resulting 3D profile of the initially produced quark–gluon plasma (QGP), in which the arrows indicate the pressure gradients. **f**, The 3D profile of the QGP at the end of the hydrodynamic expansion before it freezes out into particles, in which the arrows indicate the velocities of fluid cells. **g**, Charged particle tracks measured in the detector. The timescales shown are in units of fm/c—the time for light to travel 1 femtometre. The body–body configuration has large eccentricity ε_2 and small gradient $d_\perp$, leading to large elliptic flow v_2 and smaller average transverse momentum $[p_T]$ and vice versa for tip–tip configuration (see main text).

seemingly impossible task of 'figuring out a pocket watch by smashing two together and observing the flying debris'. The collective response plays a key part.

Our shape-imaging technique focuses on head-on (near-zero impact parameter) collisions of prolate-deformed nuclei (Fig. 1d–g). The initial configurations lie between two extremes: body–body (top) and tip–tip (bottom) collisions (Fig. 1d). Before impact, Lorentz contraction flattens the ground-state nuclei into pancake-like shapes by a factor of $\Gamma = \frac{1}{2}\sqrt{s_{\mathrm{NN}}}/m_0 > 100$, where $m_0 \approx 0.94$ GeV is the nucleon mass (Fig. 1e). The initial impact, lasting $\tau_{\mathrm{expo}} = 2R_0/\Gamma \lesssim 0.1$ fm/c, acts as an exposure time. The shape and size of the overlap region, reflecting the initially produced QGP, directly mirror those of the colliding nuclei projected on the transverse (xy) plane (Fig. 1e). Body–body collisions create a larger, elongated QGP, which undergoes pressure-gradient-driven expansion (indicated by arrows) until about 10 fm/c (ref. 7), resulting in an inverted, asymmetric distribution (Fig. 1f). By contrast, tip–tip collisions form a compact, circular QGP, driving a more rapid but symmetric expansion (Fig. 1f). In the final stage, the QGP freezes into thousands of particles, captured as tracks in detectors, whose angular distributions reflect the initial QGP shape (Fig. 1g). This flow-assisted imaging is similar to the Coulomb explosion imaging in molecule structure analysis[17–21], in which the spatial arrangement of atoms, ionized by an X-ray laser or through a passage in thin foils, is deduced from their mutual Coulomb-repulsion-driven expansion. However, the expansion duration in high-energy collisions is 10^6–10^9 times shorter.

The concept that the dynamics of QGP can be used to image the geometrical properties of its initial condition was widely recognized. This understanding has facilitated the determination of the impact parameter and fluctuations in nucleon positions[7], as well as the neutron skin of the colliding nuclei[22], by measuring higher-order harmonic flows. However, our study took a further step to image the shape of the colliding nuclei through their impact on the initial condition.

Energy evolution of shapes

A pertinent question is how the shapes observed in high-energy colliders compare with those derived from low-energy experiments. For well-deformed nuclei such as ^{238}U, we expect them to align at a basic level. However, there are other correlations (such as clustering and short-range correlations) that manifest at increasingly faster timescales from 1,000 to a few fm/c. Moreover, high-energy collisions also probe nuclear structure at sub-nucleonic levels, such as quark and gluon correlations, as well as modifications caused by dense gluon fields[23]. As a result, the deformations observed at high energy may differ from those at low energy, motivating us to examine nuclear phenomena across energy scales and discover new phenomena.

Observables

In Fig. 1e, the initial shape of QGP is quantified by the eccentricity, $\varepsilon_2 = \frac{\langle y^2\rangle - \langle x^2\rangle}{\langle y^2\rangle + \langle x^2\rangle}$, calculated from the nucleon distribution in the

xy-plane, perpendicular to the beam direction. The hydrodynamic expansion, reacting to ε_2, results in particle anisotropy, described as $dN/d\phi \propto 1 + 2v_2\cos(2\phi)$ aligned with the impact parameter along the x-axis. This phenomenon, known as elliptic flow (v_2) (ref. 24), is shown in Fig. 1g. Moreover, the compactness of the QGP, indicated by the inverse area of the overlap $d_\perp \propto 1/\sqrt{\langle x^2\rangle\langle y^2\rangle}$ (ref. 25), influences the radial expansion or radial flow, captured in the event-wise average transverse momentum ($[p_T]$). A key discovery at RHIC was the behaviour of QGP as a nearly perfect, inviscid fluid[26,27], effectively transforming initial geometry into final state anisotropies. Hydrodynamic models have confirmed linear response relations: $v_2 \propto \varepsilon_2$ (ref. 28) and $\delta p_T \propto \delta d_\perp$ (ref. 29), where $\delta p_T = [p_T] - \langle[p_T]\rangle$ and $\delta d_\perp = d_\perp - \langle d_\perp\rangle$ denote event-wise deviations from mean values.

In head-on collisions with spherical nuclei, non-zero ε_2 and $\delta d_\perp$ can be generated by the random fluctuations in the position of nucleons in the overlap region. In non-head-on collisions, apart from these stochastic elements, the overlap region also has an average elliptical shape. This average shape significantly contributes to ε_2, known as reaction plane eccentricity $\varepsilon_2^{\mathrm{rp}}$ (ref. 30) but has little effect on the radial quantity $\delta d_\perp$.

Prolate deformation further modifies ε_2 and $d_\perp$. Body–body collisions in this context yield high ε_2 and low $d_\perp$ values and vice versa for tip–tip collisions. This leads to enhanced, anti-correlated event-by-event fluctuations in ε_2 and $d_\perp$ (ref. 31), measurable through observables such as $\langle v_2^2\rangle$, $\langle(\delta p_T)^2\rangle$ and $\langle v_2^2\delta p_T\rangle$ (ref. 32) that are linearly related to the moments of the initial condition $\langle\varepsilon_2^2\rangle$, $\langle(\delta d_\perp)^2\rangle$ and $\langle\varepsilon_2^2\delta d_\perp\rangle$. These observables, linked to two- and three-body nucleon distributions in the intrinsic frame (Methods), were found to have a simple parametric dependence on shape parameters[33]:

$$\begin{aligned}\langle v_2^2\rangle &= a_1 + b_1\beta_2^2,\\ \langle(\delta p_T)^2\rangle &= a_2 + b_2\beta_2^2,\\ \langle v_2^2\delta p_T\rangle &= a_3 - b_3\beta_2^3\cos(3\gamma).\end{aligned} \tag{2}$$

The positive coefficients a_n and b_n capture the collision geometry and QGP properties. The b_n values are nearly independent of the impact parameter, whereas a_n values are minimized in head-on collisions, making these collisions ideal for constraining nuclear shape. Our study offers the first quantitative and simultaneous determination of β_2 and γ using all three observables in equation (2).

Nuclear shapes from low-energy data

Our measurements use data from high-energy ^{238}U + ^{238}U and ^{197}Au + ^{197}Au collisions. These species have contrasting shapes: mildly oblate ^{197}Au (close to magic numbers with $Z = 79$ protons and $N = 118$ neutrons) and highly prolate ^{238}U (an open shell nucleus with 92 protons and 146 neutrons). This comparison helps us to deduce the shape of ^{238}U. A state-of-the-art beyond the mean-field model, which reproduces the bulk of experimental data on ^{197}Au, predicts deformation values of $\beta_{2\mathrm{Au}} \approx 0.12$–$0.14$ and $\gamma_{\mathrm{Au}} \approx 43°$ (ref. 34). The deformation of ^{238}U, inferred from measured transition rates within rotational spectra, is estimated to be $\beta_{2\mathrm{U}} = 0.287 \pm 0.007$ (ref. 35).

Experimental estimates of the Uranium triaxiality have been derived from energy levels and transition data under a rigid-rotor assumption, suggesting $\gamma_{\mathrm{U}} = 6°$–$8°$ (ref. 36). An important issue concerns the softness of γ: whether the nuclei have rigid triaxial shape or fluctuations of γ around its mean value[37]. This issue is complicated by possible changes of γ when nuclei are excited[38]. Our three-body observable $\langle v_2^2\delta p_T\rangle$ in equation (2) is sensitive only to the mean of the triaxiality, not its fluctuations[39]. Nevertheless, measuring $\beta_{2\mathrm{U}}$ and γ_{U} could validate our imaging method and investigate its ground-state triaxiality.

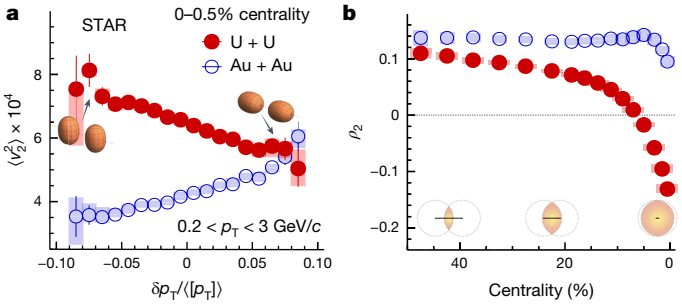

Fig. 2 | Correlation between elliptic flow and radial flow. a, $\langle v_2^2\rangle$ versus $\delta p_T/\langle[p_T]\rangle$ in 0–0.5% most central Au + Au and U + U collisions. **b**, $\rho_2 = \langle v_2^2\delta p_T\rangle/(\langle v_2^2\rangle\sqrt{\langle(\delta p_T)^2\rangle})$ across centrality, quantifying the strength of v_2–δp_T correlation. The elliptic-shaped overlaps in the transverse plane for various centralities are also shown.

Experimental setup and results

Our analysis uses U + U data from 2012 and Au + Au data from 2010 and 2011 at $\sqrt{s_{\mathrm{NN}}} = 193$ GeV and 200 GeV, respectively, using the STAR detector at RHIC. Each collision produces up to 2,000 charged particles in the STAR time-projection chamber (TPC)[40], covering the polar angle range $|\theta - 90°| \lesssim 50°$ and full ϕ range. The TPC tracks these particles and determines their p_T. Collision events are categorized by centrality, defined as the percentage of the total inelastic cross-section, with lower percentages indicating a larger number of created particles. We calculate $\langle v_2^2\rangle$, $\langle(\delta p_T)^2\rangle$ and $\langle v_2^2\delta p_T\rangle$ by established methods[41] using tracks in $0.2 < p_T < 3$ GeV/c. The results incorporate the uncertainties arising from track selection, reconstruction efficiency, background events and correlations unrelated to flow (Methods).

To directly observe the shape–size correlation shown in Fig. 1e,f, we analyse the 0–0.5% most central collisions and correlate $\langle v_2^2\rangle$ with event-wise δp_T values (Fig. 2a). A pronounced anticorrelation in U + U collisions aligns with the expectation[31]: events with small δp_T are enriched with body–body collisions and large δp_T are enriched with tip–tip collisions. This effect is striking, as $\langle v_2^2\rangle$ in U + U is twice that of Au + Au at the lowest δp_T, yet similar at the highest δp_T.

We quantify this correlation using normalized covariance $\rho_2 = \langle v_2^2\delta p_T\rangle/(\langle v_2^2\rangle\sqrt{\langle(\delta p_T)^2\rangle})$ (Fig. 2b). In Au + Au collisions, ρ_2 is relatively constant, with a minor decrease in the central region because of centrality smearing[42]. This smearing can be reduced by averaging over a wider, say 0–5% centrality range[43]. By contrast, ρ_2 in U + U collisions decreases steadily, turning negative at about 7% centrality, reflecting the large prolate deformation of ^{238}U. The deformation has the greatest impact on central collisions but also influences other centrality ranges.

Observables in a collision system are strongly influenced by QGP properties during hydrodynamic evolution. By taking ratios between the two systems, these final state effects are largely mitigated: $R_{\mathcal{O}} = \langle\mathcal{O}\rangle_{\mathrm{U+U}}/\langle\mathcal{O}\rangle_{\mathrm{Au+Au}}$ (Methods). Figure 3a–c shows ratios for the three observables. $R_{v_2^2}$ and $R_{(\delta p_T)^2}$ increase by up to 60% in central collisions, requiring a large $\beta_{2\mathrm{U}}$, whereas $R_{v_2^2\delta p_T}$ decreases by up to threefold across centralities, demanding a large $\beta_{2\mathrm{U}}$ and a small γ_{U}. The ratios in the 0–5% most central range, having the greatest sensitivity to ^{238}U shape, are shown as hatch bands in Fig. 3d–f.

The data are compared with the state-of-the-art IP-Glasma + MUSIC hydrodynamic model[25,44], which combines the fluctuating initial energy density distributions, relativistic viscous hydrodynamics and hadronic transport. This model, successful in describing flow observables at both RHIC and the LHC[44], parameterizes nuclear shapes with a deformed Woods–Saxon profile,

$$\rho(r,\theta,\phi) \propto [1 + \exp(r - R(\theta,\phi))/a]^{-1}. \tag{3}$$

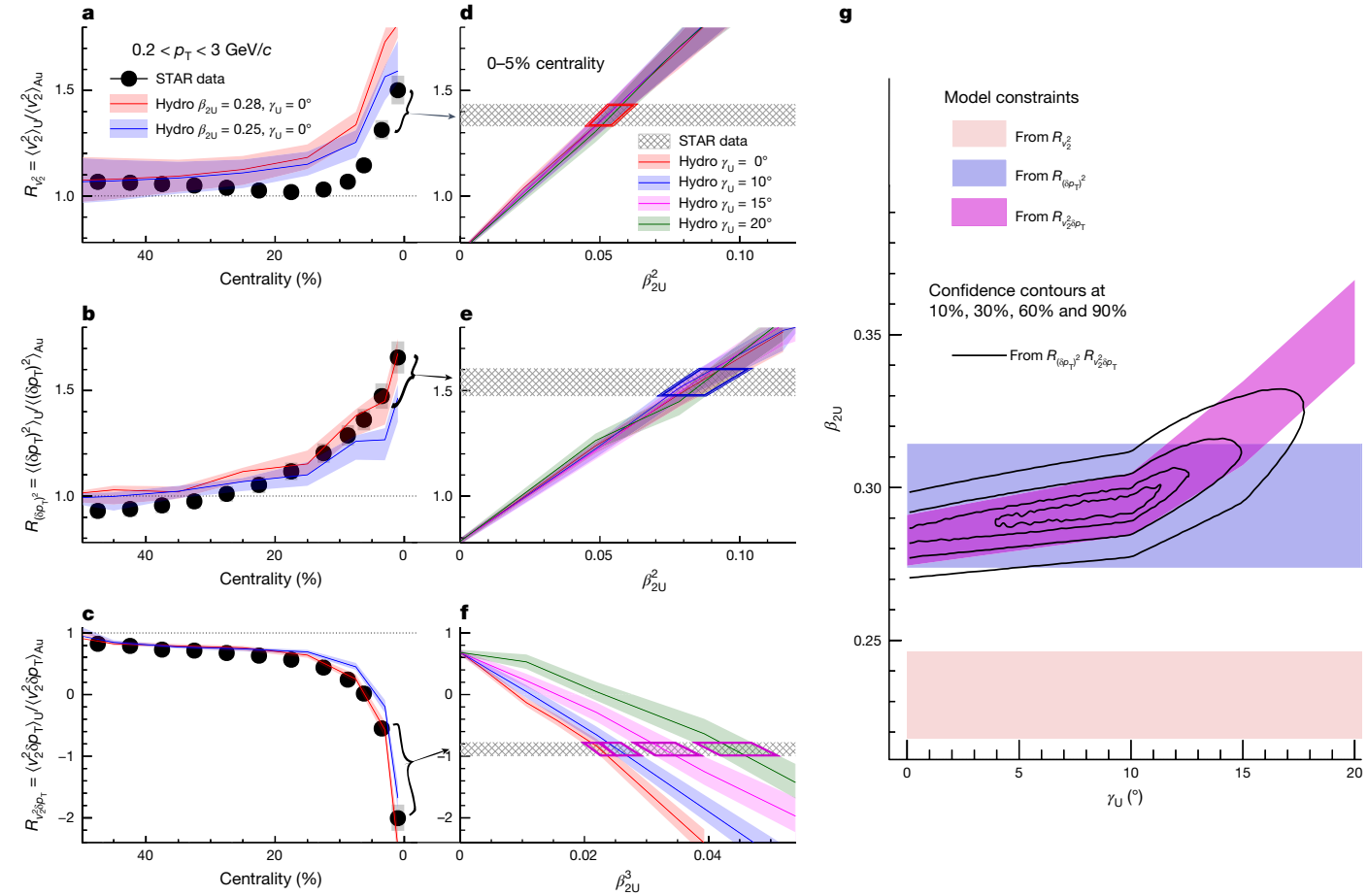

Fig. 3 | Constraining the shape of ^{238}U. a–c, Ratios of $\langle v_2^2\rangle$ (**a**), $\langle(\delta p_T)^2\rangle$ (**b**) and $\langle v_2^2\delta p_T\rangle$ (**c**) between U + U and Au + Au collisions as a function of centrality. The data are compared with the IP-Glasma + MUSIC hydrodynamic model calculation assuming $\beta_{2U} = 0.28$ (red) and $\beta_{2U} = 0.25$ (blue), the shaded bands of which denote the model uncertainties (Methods). **d–f**, Ratio values in 0–5% most central collisions (hatch bands) for $\langle v_2^2\rangle$ (**d**), $\langle(\delta p_T)^2\rangle$ (**e**) and $\langle v_2^2\delta p_T\rangle$ (**f**) are compared with model calculations as a function of β_{2U}^2 or β_{2U}^3 for four γ_U values. The coloured quadrilaterals delineate the allowed ranges of β_{2U}^2 or β_{2U}^3 from this data-model comparison. **g**, The constrained ranges of (β_{2U},γ_U) from three observables separately, and the confidence contours obtained by combining $\langle(\delta p_T)^2\rangle$ and $\langle v_2^2\delta p_T\rangle$ (solid lines). The constraint from $R_{v_2^2}$ is viewed as a lower limit and hence is not used (see main text).

The parameters for Au are fixed to an oblate shape with $\beta_{2Au} = 0.14$ and $\gamma_{Au} = 45°$ (ref. 34), whereas those for U are varied. The model also considers final state effects by adjusting QGP viscosities and initial condition uncertainties, including variations in nuclear radius R_0, skin a, β_{2Au}, γ_{Au} and higher-order shapes (Extended Data Table 1). These variations are included in the model uncertainties. The mass numbers of Au and U, differing by only 20%, result in almost completely cancelling final state effects, leaving model uncertainties mainly from initial conditions. In Fig. 3a–c, calculations for $\beta_{2U} = 0.28$ match central data for $R_{(\delta p_T)^2}$ and $R_{v_2^2\delta p_T}$, but overestimate $R_{v_2^2}$ in 0–30% centrality. This overestimation stems from the limitations of the model in describing ε_2^{rp}-induced v_2 components, which are strongly affected by variations in the impact parameter and other structural parameters such as nuclear radius and skin[45] and possible longitudinal flow decorrelations[46]. Thus, the $R_{v_2^2}$ comparison is expected to set only a lower bound for β_{2U} in this model.

In Fig. 3d–f, we contrast the 0–5% central data against predictions for varying β_{2U} and γ_U. Calculated $R_{v_2^2}$ and $R_{(\delta p_T)^2}$ change linearly with β_{2U}^2, whereas $R_{v_2^2\delta p_T}$ follows a $\beta_{2U}^3\cos(3\gamma_U)$ trend, aligning remarkably with equation (2). The intersections between data and model delineate preferred β_{2U} ranges, yielding $\beta_{2U}(R_{(\delta p_T)^2}) = 0.294 \pm 0.021$ and a lower limit value $\beta_{2U}(R_{v_2^2}) = 0.234 \pm 0.014$. For $R_{v_2^2\delta p_T}$, the favoured β_{2U} range varies with γ_U. These preferred ranges are shown in Fig. 3g. A combined analysis of constraints from $R_{(\delta p_T)^2}$ and $R_{v_2^2\delta p_T}$ is performed, yielding $\beta_{2U} = 0.297 \pm 0.015$ and $\gamma_U = 8.5° \pm 4.8°$ (mean and 1 standard deviation, see Methods).

The data are also compared with Trajectum[22], another hydrodynamic model with a different implementation of the initial condition and QGP evolution. Trajectum derives constraints on the initial and final state parameters of the QGP based on a Bayesian analysis of the LHC data that are then extrapolated to the RHIC energies. These constraints were not tuned to the RHIC data but are nevertheless useful in estimating the theoretical uncertainties. The relevant constraints are $\beta_{2U} = 0.275 \pm 0.017$ and $\gamma_U = 15.5° \pm 7.8°$. A combination of constraints from the two models yields $\beta_{2U} = 0.286 \pm 0.025$ and $\gamma_U = 8.7° \pm 4.5°$ (Methods).

The extracted β_{2U} value is in line with low-energy estimates[35], implying other sources of nucleon, quark and gluon correlations in ^{238}U are less impactful compared with its large deformation, as supported by recent model studies[23]. Meanwhile, the small γ_U value excludes a large triaxiality of uranium and indicates an average value remarkably consistent with the low-energy estimate based on a similar rigid-rotor assumption. This marks the first extraction of nuclear ground-state triaxiality without involving transitions to excited states.

Applications

The flow-assisted nuclear shape imaging is a promising tool for exploring the structure of atomic nuclei in their ground state. The strength

of this method lies in capturing a fast snapshot of nucleon spatial distribution, applicable to any collision species. This contrasts with nuclear spectroscopy, in which complexity varies with the position of the nucleus on the Segrè chart. This approach is effective for discerning shape differences between species with similar mass numbers, ideally isobar pairs. Many applications are possible, with a few examples given here:

1. Odd-mass nuclides: for odd-mass nuclei, where either N or Z is odd, the nuclear shapes should be similar to adjacent even–even nuclei. As the transition data are more complex[1,3], the ground-state shapes are usually inferred from the data measured by laser spectroscopy method[5]. The high-energy approach is suitable for both odd-mass nuclei and even–even nuclei, hence eliminating a possible source of bias in low-energy experiments.
2. Octupole and hexadecapole deformations: these less common and generally weaker deformations[47] can be probed through measurement of higher-order flow harmonics (triangular and quadrangular flows).
3. Dynamic deformations in soft nuclei: this method could distinguish between average deformation and transient shape fluctuations using measurements of multi-particle correlations[39]. For example, the sixth-particle correlator $\langle v_2^6 \rangle$ has direct sensitivity to the fluctuations of γ. This information was obtained in rare cases at low energy[48,49]. Our technique, sensitive only to the ground state, also sidesteps the complexities of disentangling shape variations during transitions to excited states.
4. $0\nu\beta\beta$ decay: the decay rate hinges on nuclear matrix elements (NME), significantly affected by the shapes of the initial and final species—a pair of isobars with the same mass number. Present NME uncertainties, partly stemming from inadequate knowledge of nuclear shapes, pose a main challenge in experimental design[12]. This method, tailored for isobars, allows for precisely determining shape differences between these species. This could reduce NME uncertainties, and hence aid in experiments searching for $0\nu\beta\beta$ decay and enhance our understanding of neutrino properties.

It would be remiss not to mention that our approach also holds promise in advancing the study of QGP, particularly its dynamics and transport properties, which have been limited by a poor understanding of QGP initial conditions[6,7] (Fig. 1e). By contrasting flow observables in similarly massed but structurally different species, our technique effectively eliminates final state effects, thereby isolating initial condition variations seeded by shape differences. This can explain the mechanisms of initial condition formation and consequently help to improve QGP transport property extraction through Bayesian inferences[50–52] and lead to breakthroughs in high-energy nuclear physics.

Collective-flow-assisted nuclear shape imaging is a discovery tool for exploring nuclear structure and high-energy nuclear collision physics. Future research could leverage colliders to conduct experiments with selected isobaric or isobar-like pairs. The combination of high- and low-energy techniques enables interdisciplinary research in the study of atomic nuclei across energy scales.

Online content

Any methods, additional references, Nature Portfolio reporting summaries, source data, extended data, supplementary information, acknowledgements, peer review information; details of author contributions and competing interests; and statements of data and code availability are available at https://doi.org/10.1038/s41586-024-08097-2.

1. Bohr, A. & Mottelson, B. R. *Nuclear Structure* Vol. 1 (World Scientific, 1998).
2. Heyde, K. & Wood, J. L. Nuclear shapes: from earliest ideas to multiple shape coexisting structures. *Phys. Scr.* **91**, 083008 (2016).
3. Bohr, A. & Mottelson, B. R. *Nuclear Structure* Vol. 2 (World Scientific, 1998).
4. Cline, D. Nuclear shapes studied by coulomb excitation. *Annu. Rev. Nucl. Part. Sci.* **36**, 683–716 (1986).
5. Yang, X. F., Wang, S. J., Wilkins, S. G. & Garcia Ruiz, R. F. Laser spectroscopy for the study of exotic nuclei. *Prog. Part. Nucl. Phys.* **129**, 104005 (2023).
6. Shuryak, E. Strongly coupled quark-gluon plasma in heavy ion collisions. *Rev. Mod. Phys.* **89**, 035001 (2017).
7. Busza, W., Rajagopal, K. & van der Schee, W. Heavy ion collisions: the big picture and the big questions. *Annu. Rev. Nucl. Part. Sci.* **68**, 339–376 (2018).
8. Hofstadter, R. Electron scattering and nuclear structure. *Rev. Mod. Phys.* **28**, 214–254 (1956).
9. Möller, P., Sierk, A. J., Ichikawa, T. & Sagawa, H. Nuclear ground-state masses and deformations: FRDM(2012). *At. Data Nucl. Data Tables* **109–110**, 1–204 (2016).
10. Schatz, H. et al. rp-Process nucleosynthesis at extreme temperature and density conditions. *Phys. Rep.* **294**, 167–263 (1998).
11. Schunck, N. & Regnier, D. Theory of nuclear fission. *Prog. Part. Nucl. Phys.* **125**, 103963 (2022).
12. Engel, J. & Menéndez, J. Status and future of nuclear matrix elements for neutrinoless double-beta decay: a review. *Rep. Prog. Phys.* **80**, 046301 (2017).
13. Toh, Y. et al. Evidence for rigid triaxial deformation at low energy in ^{76}Ge. *Phys. Rev. C* **87**, 041304 (2013).
14. Nakatsukasa, T., Matsuyanagi, K., Matsuo, M. & Yabana, K. Time-dependent density-functional description of nuclear dynamics. *Rev. Mod. Phys.* **88**, 045004 (2016).
15. Heyde, K. & Wood, J. L. Shape coexistence in atomic nuclei. *Rev. Mod. Phys.* **83**, 1467–1521 (2011).
16. Bender, M., Heenen, P.-H. & Reinhard, P.-G. Self-consistent mean-field models for nuclear structure. *Rev. Mod. Phys.* **75**, 121–180 (2003).
17. Vager, Z., Naaman, R. & Kanter, E. P. Coulomb explosion imaging of small molecules. *Science* **244**, 426–431 (1989).
18. Kunitski, M. et al. Observation of the Efimov state of the helium trimer. *Science* **348**, 551–555 (2015).
19. Endo, T. et al. Capturing roaming molecular fragments in real time. *Science* **370**, 1072–1077 (2020).
20. Boll, R. et al. X-ray multiphoton-induced coulomb explosion images complex single molecules. *Nat. Phys.* **18**, 423–428 (2022).
21. Miller, J. L. Coulomb-explosion imaging tackles an 11-atom molecule. *Phys. Today* **75**, 12–14 (2022).
22. Giacalone, G., Nijs, G. & van der Schee, W. Determination of the neutron skin of ^{208}Pb from ultrarelativistic nuclear collisions. *Phys. Rev. Lett.* **131**, 202302 (2023).
23. Mäntysaari, H., Schenke, B., Shen, C. & Zhao, W. Multiscale imaging of nuclear deformation at the electron-ion collider. *Phys. Rev. Lett.* **131**, 062301 (2023).
24. Ollitrault, J.-Y. Anisotropy as a signature of transverse collective flow. *Phys. Rev. D* **46**, 229–245 (1992).
25. Schenke, B., Shen, C. & Teaney, D. Transverse momentum fluctuations and their correlation with elliptic flow in nuclear collisions. *Phys. Rev. C* **102**, 034905 (2020).
26. STAR Collaboration. Experimental and theoretical challenges in the search for the quark–gluon plasma: the STAR Collaboration's critical assessment of the evidence from RHIC collisions. *Nucl. Phys. A* **757**, 102–183 (2005).
27. PHENIX Collaboration. Formation of dense partonic matter in relativistic nucleus-nucleus collisions at RHIC: experimental evaluation by the PHENIX collaboration. *Nucl. Phys. A* **757**, 184–283 (2005).
28. Niemi, H., Denicol, G. S., Holopainen, H. & Huovinen, P. Event-by-event distributions of azimuthal asymmetries in ultrarelativistic heavy-ion collisions. *Phys. Rev. C* **87**, 054901 (2013).
29. Bożek, P. & Broniowski, W. Transverse-momentum fluctuations in relativistic heavy-ion collisions from event-by-event viscous hydrodynamics. *Phys. Rev. C* **85**, 044910 (2012).
30. Alver, B. et al. Importance of correlations and fluctuations on the initial source eccentricity in high-energy nucleus-nucleus collisions. *Phys. Rev. C* **77**, 014906 (2008).
31. Giacalone, G. Observing the deformation of nuclei with relativistic nuclear collisions. *Phys. Rev. Lett.* **124**, 202301 (2020).
32. Bozek, P. Transverse-momentum–flow correlations in relativistic heavy-ion collisions. *Phys. Rev. C* **93**, 044908 (2016).
33. Jia, J. Probing triaxial deformation of atomic nuclei in high-energy heavy ion collisions. *Phys. Rev. C* **105**, 044905 (2022).
34. Bally, B., Giacalone, G. & Bender, M. The shape of gold. *Eur. Phys. J. A* **59**, 58 (2023).
35. Pritychenko, B., Birch, M., Singh, B. & Horoi, M. Tables of E2 transition probabilities from the first 2^+ states in even–even nuclei. *At. Data Nucl. Data Tables* **107**, 1–139 (2016).
36. Wu, C. Y. & Cline, D. Triaxiality in quadrupole deformed nuclei. *Phys. Rev. C* **54**, 2356–2360 (1996).
37. Sharpey-Schafer, J. F., Bark, R. A., Bvumbi, S. P., Dinoko, T. R. S. & Majola, S. N. T. "Stiff" deformed nuclei, configuration dependent pairing and the β and γ degrees of freedom. *Eur. Phys. J. A* **55**, 15 (2019).
38. Otsuka, T. et al. Prevailing triaxial shapes in heavy nuclei driven by nuclear tensor force. Preprint at arxiv.org/abs/2303.11299 (2023).
39. Dimri, A., Bhatta, S. & Jia, J. Impact of nuclear shape fluctuations in high-energy heavy ion collisions. *Eur. Phys. J. A* **59**, 45 (2023).
40. Anderson, M. et al. The Star time projection chamber: a unique tool for studying high multiplicity events at RHIC. *Nucl. Instrum. Methods Phys. Res. A* **499**, 659–678 (2003).
41. Bilandzic, A., Snellings, R. & Voloshin, S. Flow analysis with cumulants: direct calculations. *Phys. Rev. C* **83**, 044913 (2011).
42. Aad, G. et al. Correlations between flow and transverse momentum in Xe+Xe and Pb+Pb collisions at the LHC with the ATLAS detector: a probe of the heavy-ion initial state and nuclear deformation. *Phys. Rev. C* **107**, 054910 (2023).
43. Zhou, M. & Jia, J. Centrality fluctuations in heavy-ion collisions. *Phys. Rev. C* **98**, 044903 (2018).
44. Schenke, B., Shen, C. & Tribedy, P. Running the gamut of high energy nuclear collisions. *Phys. Rev. C* **102**, 044905 (2020).

45. Jia, J., Giacalone, G. & Zhang, C. Separating the Impact of Nuclear Skin and Nuclear Deformation in High-Energy Isobar Collisions. *Phys. Rev. Lett.* **131**, 022301 (2023).
46. Jia, J., Huang, S., Zhang, C. & Bhatta, S. Sources of longitudinal flow decorrelations in high-energy nuclear collisions. Preprint at arxiv.org/abs/2408.15006 (2024).
47. Butler, P. A. & Nazarewicz, W. Intrinsic reflection asymmetry in atomic nuclei. *Rev. Mod. Phys.* **68**, 349–421 (1996).
48. Wu, C. Y. et al. Quadrupole collectivity and shapes of Os/Pt nuclei. *Nucl. Phys. A* **607**, 178–234 (1996).
49. Ayangeakaa, A. D. et al. Evidence for rigid triaxial deformation in ^{76}Ge from a model-independent analysis. *Phys. Rev. Lett.* **123**, 102501 (2019).
50. Bernhard, J. E., Moreland, J. S. & Bass, S. A. Bayesian estimation of the specific shear and bulk viscosity of quark–gluon plasma. *Nat. Phys.* **15**, 1113–1117 (2019).
51. Everett, D. et al. Phenomenological constraints on the transport properties of QCD matter with data-driven model averaging. *Phys. Rev. Lett.* **126**, 242301 (2021).
52. Nijs, G., van der Schee, W., Gürsoy, U. & Snellings, R. Transverse momentum differential global analysis of heavy-ion collisions. *Phys. Rev. Lett.* **126**, 202301 (2021).

STAR Collaboration

M. I. Abdulhamid[1], B. E. Aboona[2], J. Adam[3], J. R. Adams[4], G. Agakishiev[5], I. Aggarwal[6], M. M. Aggarwal[6], Z. Ahammed[7], A. Aitbaev[5], I. Alekseev[8,9], E. Alpatov[9], A. Aparin[5], S. Aslam[10], J. Atchison[11], G. S. Averichev[5], V. Bairathi[12], J. G. Ball Cap[13], K. Barish[14], P. Bhagat[15], A. Bhasin[15], S. Bhatta[16], S. R. Bhosale[17], I. G. Bordyuzhin[8], J. D. Brandenburg[4], A. V. Brandin[9], C. Broodo[13], X. Z. Cai[18], H. Caines[19], M. Calderón de la Barca Sánchez[20], D. Cebra[20], J. Ceska[3], I. Chakaberia[21], B. K. Chan[22], Z. Chang[23], A. Chatterjee[24], D. Chen[14], J. Chen[25], J. H. Chen[26], Z. Chen[25], J. Cheng[27], Y. Cheng[22], W. Christie[28], X. Chu[28], H. J. Crawford[29], M. Csanád[17], G. Dale-Gau[30], A. Das[3], T. G. Dedovich[5], I. M. Deppner[31], A. A. Derevschikov[32], A. Dhamija[6], P. Dixit[33], X. Dong[21], J. L. Drachenberg[11], E. Duckworth[34], J. C. Dunlop[28], J. Engelage[29], G. Eppley[35], S. Esumi[36], O. Evdokimov[30], O. Eyser[28], R. Fatemi[37], S. Fazio[38], C. J. Feng[39], Y. Feng[40], E. Finch[41], Y. Fisyak[28], F. A. Flor[19], C. Fu[42], T. Gao[25], F. Geurts[35], N. Ghimire[43], A. Gibson[44], K. Gopal[45], X. Gou[25], D. Grosnick[44], A. Gupta[15], A. Hamed[1], Y. Han[35], M. D. Harasty[20], J. W. Harris[19], H. Harrison-Smith[37], W. He[26], X. H. He[42], Y. He[25], C. Hu[46], Q. Hu[42], Y. Hu[21], H. Huang[39], H. Z. Huang[22], S. L. Huang[16], T. Huang[30], Y. Huang[27], Y. Huang[47], T. J. Humanic[4], M. Isshiki[36], W. W. Jacobs[23], A. Jalotra[15], C. Jena[45], Y. Ji[21], J. Jia[16,28], C. Jin[35], X. Ju[48], E. G. Judd[29], S. Kabana[12], D. Kalinkin[37], K. Kang[27], D. Kapukchyan[14], K. Kauder[28], D. Keane[34], A. Kechechyan[5], A. Khanal[49], A. Kiselev[28], A. G. Knospe[50], H. S. Ko[21], L. Kochenda[9], A. A. Korobitsin[5], A. Yu. Kraeva[9], P. Kravtsov[9], L. Kumar[6], M. C. Labonte[20], R. Lacey[16], J. M. Landgraf[28], A. Lebedev[28], R. Lednicky[5], J. H. Lee[28], Y. H. Leung[31], C. Li[47], D. Li[48], H-S. Li[40], H. Li[51], W. Li[35], X. Li[48], Y. Li[48], Y. Li[27], Z. Li[48], X. Liang[14], Y. Liang[34], T. Lin[25], Y. Lin[52], C. Liu[42], G. Liu[53], H. Liu[47], L. Liu[47], T. Liu[19], X. Liu[4], Y. Liu[2], Z. Liu[47], T. Ljubicic[35], O. Lomicky[3], R. S. Longacre[28], E. M. Loyd[14], T. Lu[42], J. Luo[48], X. F. Luo[47], V. B. Luong[5], L. Ma[26], R. Ma[28], Y. G. Ma[26], N. Magdy[16], R. Manikandhan[13], S. Margetis[34], O. Matonoha[3], G. McNamara[49], O. Mezhanska[3], K. Mi[47], N. G. Minaev[32], B. Mohanty[54], B. Mondal[54], M. M. Mondal[54], I. Mooney[19], D. A. Morozov[32], A. Mudrokh[5], M. I. Nagy[17], A. S. Nain[6], J. D. Nam[43], M. Nasim[33], E. Nedorezov[5], D. Neff[22], J. M. Nelson[29], M. Nie[25], G. Nigmatkulov[30], T. Niida[36], L. V. Nogach[32], T. Nonaka[36], G. Odyniec[21], A. Ogawa[28], S. Oh[55], V. A. Okorokov[9], K. Okubo[36], B. S. Page[28], S. Pal[3], A. Pandav[21], A. Panday[33], Y. Panebratsev[5], T. Pani[56], P. Parfenov[9], A. Paul[14], C. Perkins[29], B. R. Pokhrel[43], M. Posik[43], A. Povarov[9], T. Protzman[50], N. K. Pruthi[6], J. Putschke[49], Z. Qin[27], H. Qiu[42], C. Racz[14], S. K. Radhakrishnan[34], A. Rana[6], R. L. Ray[57], C. W. Robertson[40], O. V. Rogachevsky[5], M. A. Rosales Aguilar[37], D. Roy[56], L. Ruan[28], A. K. Sahoo[33], N. R. Sahoo[45], H. Sako[36], S. Salur[56], E. Samigullin[8], S. Sato[36], B. C. Schaefer[50], W. B. Schmidke[28,66], N. Schmitz[58], J. Seger[59], R. Seto[14], P. Seyboth[58], N. Shah[10], E. Shahaliev[5], P. V. Shanmuganathan[28], T. Shao[26], M. Sharma[15], N. Sharma[33], R. Sharma[45], S. R. Sharma[45], A. I. Sheikh[34], D. Shen[25], D. Y. Shen[26], K. Shen[48], S. S. Shi[47], Y. Shi[25], Q. Y. Shou[26], F. Si[48], J. Singh[12], S. Singha[42], P. Sinha[45], M. J. Skoby[40,60], Y. Söhngen[31], Y. Song[19], B. Srivastava[40], T. D. S. Stanislaus[44], D. J. Stewart[49], M. Strikhanov[9], Y. Su[48], C. Sun[16], X. Sun[42], Y. Sun[48], Y. Sun[61], B. Surrow[43], D. N. Svirida[8], Z. W. Sweger[20], A. C. Tamis[19], A. H. Tang[28], Z. Tang[48], A. Taranenko[9], T. Tarnowsky[62], J. H. Thomas[21], D. Tlusty[59], T. Todoroki[36], M. V. Tokarev[5], S. Trentalange[22], P. Tribedy[28], O. D. Tsai[22,28], C. Y. Tsang[28,34], Z. Tu[28], J. Tyler[2], T. Ullrich[28], D. G. Underwood[44,63], I. Upsal[48], G. Van Buren[28], A. N. Vasiliev[9,32], V. Verkest[49], F. Videbæk[28], S. Vokal[5], S. A. Voloshin[49], G. Wang[22], J. S. Wang[61], J. Wang[25], K. Wang[48], X. Wang[25], Y. Wang[48], Y. Wang[47], Y. Wang[27], Z. Wang[25], J. C. Webb[28], P. C. Weidenkaff[31], G. D. Westfall[62], H. Wieman[21], G. Wilks[30], S. W. Wissink[23], J. Wu[47], J. Wu[42], X. Wu[22], X. Wu[48], B. Xi[26], Z. G. Xiao[27], G. Xie[46], W. Xie[40], H. Xu[61], N. Xu[21], Q. H. Xu[25], Y. Xu[25], Y. Xu[47], Z. Xu[34], Z. Xu[22], G. Yan[25], Z. Yan[16], C. Yang[25], Q. Yang[25], S. Yang[53], Y. Yang[39], Z. Ye[53], Z. Ye[21], L. Yi[25], Y. Yu[25], W. Zha[48], C. Zhang[26], D. Zhang[53], J. Zhang[25], S. Zhang[64], W. Zhang[53], X. Zhang[42], Y. Zhang[42], Y. Zhang[48], Y. Zhang[25], Y. Zhang[52], Z. J. Zhang[39], Z. Zhang[28], Z. Zhang[30], F. Zhao[42], J. Zhao[26], M. Zhao[28], S. Zhou[47], Y. Zhou[47], X. Zhu[27], M. Zurek[28,63] & M. Zyzak[65]

[1]American University in Cairo, New Cairo, Egypt. [2]Texas A&M University, College Station, TX, USA. [3]Czech Technical University in Prague, Prague, Czech Republic. [4]The Ohio State University, Columbus, OH, USA. [5]Joint Institute for Nuclear Research, Dubna, Russia. [6]Panjab University, Chandigarh, India. [7]Variable Energy Cyclotron Centre, Kolkata, India. [8]Alikhanov Institute for Theoretical and Experimental Physics NRC 'Kurchatov Institute', Moscow, Russia. [9]National Research Nuclear University MEPhI, Moscow, Russia. [10]Indian Institute Technology, Patna, India. [11]Abilene Christian University, Abilene, TX, USA. [12]Instituto de Alta Investigación, Universidad de Tarapacá, Arica, Chile. [13]University of Houston, Houston, TX, USA. [14]University of California, Riverside, Riverside, CA, USA. [15]University of Jammu, Jammu, India. [16]Stony Brook University, Stony Brook, NY, USA. [17]Eötvös Loránd University, Budapest, Hungary. [18]Shanghai Institute of Applied Physics, Chinese Academy of Sciences, Shanghai, China. [19]Yale University, New Haven, CT, USA. [20]University of California, Davis, Davis, CA, USA. [21]Lawrence Berkeley National Laboratory, Berkeley, CA, USA. [22]University of California, Los Angeles, Los Angeles, CA, USA. [23]Indiana University, Bloomington, IN, USA. [24]National Institute of Technology Durgapur, Durgapur, India. [25]Shandong University, Qingdao, China. [26]Fudan University, Shanghai, China. [27]Tsinghua University, Beijing, China. [28]Brookhaven National Laboratory, Upton, NY, USA. [29]University of California, Berkeley, CA, USA. [30]University of Illinois at Chicago, Chicago, IL, USA. [31]University of Heidelberg, Heidelberg, Germany. [32]NRC 'Kurchatov Institute', Institute of High Energy Physics, Protvino, Russia. [33]Indian Institute of Science Education and Research, Berhampur, India. [34]Kent State University, Kent, OH, USA. [35]Rice University, Houston, TX, USA. [36]University of Tsukuba, Tsukuba, Japan. [37]University of Kentucky, Lexington, KY, USA. [38]University of Calabria & INFN-Cosenza, Rende, Italy. [39]National Cheng Kung University, Tainan City, Taiwan. [40]Purdue University, West Lafayette, IN, USA. [41]Southern Connecticut State University, New Haven, CT, USA. [42]Institute of Modern Physics, Chinese Academy of Sciences, Lanzhou, China. [43]Temple University, Philadelphia, PA, USA. [44]Valparaiso University, Valparaiso, IN, USA. [45]Indian Institute of Science Education and Research, Tirupati, India. [46]University of Chinese Academy of Sciences, Beijing, China. [47]Central China Normal University, Wuhan, China. [48]University of Science and Technology of China, Hefei, China. [49]Wayne State University, Detroit, MI, USA. [50]Lehigh University, Bethlehem, PA, USA. [51]Wuhan University of Science and Technology, Wuhan, China. [52]Guangxi Normal University, Guilin, China. [53]South China Normal University, Guangzhou, China. [54]National Institute of Science Education and Research, Jatni, India. [55]Sejong University, Seoul, South Korea. [56]Rutgers University, Piscataway, NJ, USA. [57]University of Texas, Austin, TX, USA. [58]Max-Planck-Institut für Physik, Munich, Germany. [59]Creighton University, Omaha, NE, USA. [60]Ball State University, Muncie, IN, USA. [61]Huzhou University, Huzhou, China. [62]Michigan State University, East Lansing, MI, USA. [63]Argonne National Laboratory, Argonne, IL, USA. [64]Chongqing University, Chongqing, China. [65]Frankfurt Institute for Advanced Studies FIAS, Frankfurt, Germany. [66]Deceased: W. B. Schmidke.

Methods

Accessing information in the intrinsic frame

The nuclear shape in the intrinsic frame is not directly observable in low-energy experiments. However, in high-energy collisions, the collective flow phenomenon is sensitive to the shape and size of the nucleon distribution in the overlap region of the transverse plane. This distribution, denoted as $\rho(\mathbf{r})$ with $\mathbf{r} = x + \mathrm{i}y$, provides a direct link to the shape characteristics of the two colliding nuclei in their intrinsic frames, as discussed below.

The elliptic shape of the heavy-ion initial state is characterized by its amplitude ε_2 and direction Φ_2, defined by nucleon positions as

$$\mathcal{E}_2 \equiv \varepsilon_2 e^{2i\Phi_2} = \frac{\int_{\mathbf{r}} \mathbf{r}^2 \rho(\mathbf{r})}{\int_{\mathbf{r}} |\mathbf{r}|^2 \rho(\mathbf{r})}, \int_{\mathbf{r}} = \int \mathrm{d}x\mathrm{d}y. \tag{4}$$

When the coordinate system is rotated such that x and y coincide with the minor and major axes, the elliptic eccentricity coincides with the usual definition $\varepsilon_2 = \frac{\langle y^2\rangle - \langle x^2\rangle}{\langle y^2\rangle + \langle x^2\rangle}$. The parameter ε_2 drives the elliptic flow v_2: $v_2 \propto \varepsilon_2$.

Let us now consider collisions at zero impact parameter, in which, without loss of generality, the average elliptic geometry vanishes, that is, $\langle \mathcal{E}_2 \rangle = 0$. The second moment of eccentricity over many events is given by[53,54]

$$\langle \varepsilon_2^2 \rangle = \langle \mathcal{E}_2 \mathcal{E}_2^* \rangle \approx \frac{\int_{\mathbf{r}_1,\mathbf{r}_2} (\mathbf{r}_1)^2 (\mathbf{r}_2^*)^2 \rho(\mathbf{r}_1, \mathbf{r}_2)}{\left(\int_{\mathbf{r}} |\mathbf{r}|^2 \langle \rho(\mathbf{r}) \rangle\right)^2}, \tag{5}$$

where $\langle \rho(\mathbf{r}) \rangle$ represents the event-averaged profile, and

$$\rho(\mathbf{r}_1, \mathbf{r}_2) = \langle \delta\rho(\mathbf{r}_1)\delta\rho(\mathbf{r}_2)\rangle = \langle \rho(\mathbf{r}_1)\rho(\mathbf{r}_2)\rangle - \langle \rho(\mathbf{r}_1)\rangle\langle \rho(\mathbf{r}_2)\rangle$$

is the usual two-body distribution. Similarly, the third central moments are related to the three-body distribution, $\rho(\mathbf{r}_1, \mathbf{r}_2, \mathbf{r}_3) = \langle \delta\rho(\mathbf{r}_1)\delta\rho(\mathbf{r}_2)\delta\rho(\mathbf{r}_3)\rangle$. For example,

$$\langle \varepsilon_2^2 \delta d_\perp/d_\perp \rangle \approx -\frac{\int_{\mathbf{r}_1,\mathbf{r}_2,\mathbf{r}_3} (\mathbf{r}_1)^2 (\mathbf{r}_2^*)^2 |\mathbf{r}_3^2| \rho(\mathbf{r}_1, \mathbf{r}_2, \mathbf{r}_3)}{\left(\int_{\mathbf{r}} |\mathbf{r}|^2 \langle \rho(\mathbf{r}) \rangle\right)^3}, \tag{6}$$

where we define $\delta d_\perp/d_\perp \equiv (d_\perp - \langle d_\perp \rangle)/\langle d_\perp \rangle$, and the relation $\frac{\delta d_\perp}{d_\perp} \approx -\frac{\delta\langle |\mathbf{r}^2| \rangle}{\langle |\mathbf{r}^2| \rangle} = -\frac{\int_{\mathbf{r}} |\mathbf{r}^2|\, \delta\rho(\mathbf{r})}{\int_{\mathbf{r}} |\mathbf{r}|^2\, \langle \rho(\mathbf{r}) \rangle}$ is used.

The quantities $\mathcal{E}_2$ and $\delta d_\perp/d_\perp$ depend not only on the nuclear shape but also on the random orientations of the projectile and target nuclei, denoted by Euler angles Ω_p and Ω_t. For small quadrupole deformation, it suffices to consider the leading-order forms[33]:

$$\begin{aligned} \frac{\delta d_\perp}{d_\perp} &\approx \delta_d + p_0(\Omega_p, \gamma_p)\beta_{2p} + p_0(\Omega_t, \gamma_t)\beta_{2t}, \\ \mathcal{E}_2 &\approx \mathcal{E}_0 + \mathbf{p}_2(\Omega_p, \gamma_p)\beta_{2p} + \mathbf{p}_2(\Omega_t, \gamma_t)\beta_{2t}. \end{aligned} \tag{7}$$

Here, the scalar δ_d and vector $\mathcal{E}_0$ represent values for spherical nuclei. The values of scalar p_0 and vector $\mathbf{p}_2$ are directly connected to the xy-projected one-body distribution $\rho(\mathbf{r})$. Therefore, they depend on the orientation of the two nuclei. The fluctuations of δ_d ($\mathcal{E}_0$) are uncorrelated with p_0 and the fluctuations of $\mathcal{E}_0$ are uncorrelated with $\mathbf{p}_2$. After averaging over collisions with different Euler angles and setting $\beta_{2p} = \beta_{2t}$ and $\gamma_p = \gamma_t$, we obtain

$$\begin{aligned} \langle \varepsilon_2^2 \rangle &= \langle \varepsilon_0^2 \rangle + 2\langle \mathbf{p}_2(\gamma)\mathbf{p}_2^*(\gamma)\rangle \beta_2^2 \\ \langle (\delta d_\perp/d_\perp)^2 \rangle &= \langle \delta_d^2 \rangle + 2\langle p_0(\gamma)^2 \rangle \beta_2^2 \\ \langle \varepsilon_2^2 \delta d_\perp/d_\perp \rangle &= \langle \varepsilon_0^2 \delta_d \rangle + 2\langle p_0(\gamma)\mathbf{p}_2(\gamma)\mathbf{p}_2(\gamma)^* \rangle \beta_2^3. \end{aligned} \tag{8}$$

It is found that $\langle \mathbf{p}_2(\gamma)\mathbf{p}_2^*(\gamma)\rangle$ and $\langle p_0(\gamma)^2 \rangle$ are independent of γ, while $\langle p_0(\gamma)\mathbf{p}_2(\gamma)\mathbf{p}_2(\gamma)^* \rangle \propto -\cos(3\gamma)$, resulting in expressions in equation (2).

The event-averaged moments in equation (8) are rotationally invariant and capture the intrinsic many-body distributions of $\rho(\mathbf{r})$. Note that the coefficients a_n in equation (2) are strong functions of centrality that decrease towards central collisions, whereas coefficients b_n vary weakly with centrality. Therefore, the impact of deformation is always largest in the most central collisions. In general, it can be shown that the n-particle correlations reflect the rotational invariant nth central moments of $\rho(\mathbf{r})$, which in turn are connected to the nth moments of the nuclear shape in the intrinsic frame.

Previous experimental attempts on nuclear shapes at high energy

The idea that v_2 can be enhanced by β_2 was recognized early[55–59]. Studies at RHIC[60] and the LHC[61–63] in ^{238}U + ^{238}U and ^{129}Xe + ^{129}Xe collisions indicated the influence of β_2 on v_2. Several later theoretical investigations assessed the extent to which β_2 can be constrained by v_2 alone[64–67]. A challenge with v_2 is that its a_1 term in equation (2) is affected by $\varepsilon_2^{\mathrm{rp}}$, which often exceeds the $b_1\beta_2^2$ term even in central collisions. A recent measurement of $\langle v_2^2 \delta p_\mathrm{T} \rangle$ aimed to assess the triaxiality of ^{129}Xe (ref. 42), but the extraction of γ_{Xe} was hindered by needing previous knowledge of $\beta_{2\mathrm{Xe}}$ and potentially substantial fluctuations in γ_{Xe} (refs. 39,68–71). The combination of several observables in this study allows for a more quantitative extraction of nuclear shape parameters.

Event selection

In high-energy experiments, the polar angle θ is usually mapped to the so-called pseudorapidity variable $\eta = -\ln(\tan(\theta/2))$. The STAR TPC polar angle range $|\theta - 90°| < 50°$ corresponds to $|\eta| < 1$.

The collision events are selected by requiring a coincidence of signals from two vertex position detectors on each side of the STAR barrel, covering a pseudorapidity range of $4.4 < |\eta| < 4.9$. To increase the statistics for ultra-central collision (UCC) events, a special sample of Au + Au data in 2010 and U + U data is chosen based on the criteria of high multiplicity in the STAR TPC and minimal activity in the zero-degree calorimeters that cover the beam rapidity[72].

In the offline analysis, events are selected to have collision vertices z_{vtx} within 30 cm of the TPC centre along the beamline and within 2 cm of the beam spot in the transverse plane. Furthermore, a selection criterion based on the correlation between the number of TPC tracks and the number of tracks matched to the time-of-flight detector covering $|\eta| < 0.9$ is applied to suppress pileup events (events containing more than one collision in the TPC)[73] and background events.

After applying these selection criteria, the Au + Au dataset has approximately 528 million minimum-bias events (including 370 million in 2011) and 120 million UCC events. The U + U dataset comprises around 300 million minimum-bias events and 5 million UCC events.

Track selection

For this analysis, tracks are selected with $|\eta| < 1$ and the transverse momentum range $0.2 < p_\mathrm{T} < 3.0$ GeV/c. To ensure good quality, the selected tracks must have at least 16 fit points out of a maximum of 45, and the ratio of the number of fit points to the number of possible points must be greater than 0.52. Moreover, to reduce contributions from secondary decays, the distance of the closest approach (DCA) of the track to the primary collision vertex must be less than 3 cm.

The tracking efficiency in the TPC was evaluated using the standard STAR Monte Carlo embedding technique[74]. The efficiencies are nearly independent of p_T for $p_\mathrm{T} > 0.5$ GeV/c, with plateau values ranging from 0.72 in the most central Au + Au collisions and from 0.69 in the most central U + U collisions to 0.92 in the most peripheral collisions. The efficiency exhibits some p_T-dependent variation, of the order of 10% of the plateau values, within the range of $0.2 < p_\mathrm{T} < 0.5$ GeV/c.

Centrality

The centrality of each collision is determined using $N_{\mathrm{ch}}^{\mathrm{rec}}$, which represents the number of raw reconstructed tracks in $|\eta| < 0.5$, satisfying $p_{\mathrm{T}} > 0.15$ GeV/c and having more than 10 fit points. After applying a correction to account for the dependence on the collision vertex position and the luminosity, the distribution of $N_{\mathrm{ch}}^{\mathrm{rec}}$ is compared with a Monte Carlo Glauber calculation[74]. This comparison allows for determining centrality intervals, expressed as a percentage of the total nucleus–nucleus inelastic cross-section.

Calculation of observables

The $\langle v_2^2 \rangle$, $\langle (\delta p_{\mathrm{T}})^2 \rangle$ and $\langle v_2^2 \delta p_{\mathrm{T}} \rangle$ are calculated using charged tracks as follows:

$$
\begin{aligned}
[p_{\mathrm{T}}] &= \frac{\sum_i w_i p_{\mathrm{T},i}}{\sum_i w_i}, \langle\langle p_{\mathrm{T}} \rangle\rangle \equiv \langle [p_{\mathrm{T}}] \rangle_{\mathrm{evt}} \\
\langle (\delta p_{\mathrm{T}})^2 \rangle &= \left\langle \frac{\sum_{i \neq j} w_i w_j (p_{\mathrm{T},i} - \langle\langle p_{\mathrm{T}} \rangle\rangle)(p_{\mathrm{T},j} - \langle\langle p_{\mathrm{T}} \rangle\rangle)}{\sum_{i \neq j} w_i w_j} \right\rangle_{\mathrm{evt}} \\
\langle v_2^2 \rangle &= \left\langle \frac{\sum_{i \neq j} w_i w_j \cos(2(\phi_i - \phi_j))}{\sum_{i \neq j} w_i w_j} \right\rangle_{\mathrm{evt}} \\
\langle v_2^2 \delta p_{\mathrm{T}} \rangle &= \left\langle \frac{\sum_{i \neq j \neq k} w_i w_j w_k \cos(2(\phi_i - \phi_j))(p_{\mathrm{T},k} - \langle\langle p_{\mathrm{T}} \rangle\rangle)}{\sum_{i \neq j \neq k} w_i w_j w_k} \right\rangle_{\mathrm{evt}}.
\end{aligned}
\tag{9}
$$

The averages are performed first on all multiplets within a single event and then over all events in a fixed $N_{\mathrm{ch}}^{\mathrm{rec}}$ bin. The track-wise weights $w_{i,j,k}$ account for tracking efficiency and its η and ϕ dependent variations. The values of $\langle v_2^2 \rangle$ and $\langle (\delta p_{\mathrm{T}})^2 \rangle$ are obtained using the standard method, in which particles i and j are selected from $|\eta| < 1$, as well as the two-subevent method, in which particles i and j are selected from pseudorapidity ranges of $-1 < \eta_i < -0.1$ and $0.1 < \eta_j < 1$, respectively. We also calculate the efficiency-corrected charged particle multiplicity in $|\eta| < 0.5$, defined as $N_{\mathrm{ch}} = \sum_i w_i$. This observable is used to evaluate the systematics.

The covariance $\langle v_2^2 \delta p_{\mathrm{T}} \rangle$ is calculated by averaging over all triplets labelled by particle indices i, j and k. The standard cumulant framework is used to obtain the results instead of directly calculating all triplets[41]. We also calculated $\langle v_2^2 \delta p_{\mathrm{T}} \rangle$ using the two-subevent method[42], in which particles i and j are taken from ranges of $-1 < \eta_i < -0.1$ and $0.1 < \eta_j < 1$, whereas particle k is taken from either subevents. Including a pseudorapidity gap between the particle pairs or triplets suppresses the short-range non-flow correlations arising from resonance decays and jets[75].

The calculation of $\rho_2 = \frac{\langle v_2^2 \delta p_{\mathrm{T}} \rangle}{\langle v_2^2 \rangle \sqrt{\langle (\delta p_{\mathrm{T}})^2 \rangle}}$ relies on the input values of $\langle v_2^2 \rangle$, $\langle (\delta p_{\mathrm{T}})^2 \rangle$ and $\langle v_2^2 \delta p_{\mathrm{T}} \rangle$. These components and ρ_2 are shown in Extended Data Fig. 1 as a function of centrality. In the central region, enhancements of $\langle v_2^2 \rangle$ and $\langle (\delta p_{\mathrm{T}})^2 \rangle$ are observed in U + U relative to Au + Au collisions, which is consistent with the influence of large $\beta_{2\mathrm{U}}$. By contrast, the values of $\langle v_2^2 \delta p_{\mathrm{T}} \rangle$ are markedly suppressed in U + U compared with Au + Au collisions across the entire centrality range shown. This suppression is consistent with the negative contribution expected for strong prolate deformation of U as described in equation (2).

In this analysis, the default results are obtained using the two-subevent method. The differences between the standard and two-subevent methods are used to evaluate the impact of non-flow correlations discussed below.

Influence of non-flow correlations

An important background in our measurement is non-flow: correlations among a few particles originated from a common source, such as resonance decays and jets, which are uncorrelated with the initial geometry. Two approaches are used to estimate the non-flow contributions. Non-flow correlations are short-range in η and can be suppressed by the subevent method by requiring a rapidity gap between the pairs or triplets of particles in equation (9). Hence, in the first approach, the differences between the standard and subevent methods provide an estimate of the non-flow contribution. However, part of the rapidity gap dependence of the signal in central collisions may arise from longitudinal fluctuations in $[p_{\mathrm{T}}]$ and v_2 because of variations in the initial geometry in η (ref. 42).

The second approach assumes that the clusters causing non-flow correlations are mutually independent. In this independent-source scenario, non-flow in n-particle cumulants is expected to be diluted by the charged particle multiplicity as $1/N_{\mathrm{ch}}^{n-1}$ (ref. 76). Therefore, non-flow (nf) contributions in a given centrality can be estimated by

$$
\begin{aligned}
\langle v_2^2 \rangle_{\mathrm{nf}} &\approx \frac{[\langle v_2^2 \rangle N_{\mathrm{ch}}]_{\mathrm{peri}}}{N_{\mathrm{ch}}}, \\
\langle (\delta p_{\mathrm{T}})^2 \rangle_{\mathrm{nf}} &\approx \frac{\left[\langle (\delta p_{\mathrm{T}})^2 \rangle N_{\mathrm{ch}}\right]_{\mathrm{peri}}}{N_{\mathrm{ch}}}, \\
\langle v_2^2 \delta p_{\mathrm{T}} \rangle_{\mathrm{nf}} &\approx \frac{\left[\langle v_2^2 \delta p_{\mathrm{T}} \rangle N_{\mathrm{ch}}^2\right]_{\mathrm{peri}}}{N_{\mathrm{ch}}^2}
\end{aligned}
\tag{10}
$$

where the subscript 'peri' is a label for the peripheral bin. This procedure makes two assumptions that are not fully valid: (1) the signal in the peripheral bin is all non-flow and (2) non-flow in other centralities is unmodified by final state medium effects. For example, the medium effects strongly suppress the jet yield and modify the azimuthal structure of non-flow correlations. Hence, this approach provides only a qualitative estimate of the non-flow. Moreover, this approach is not applicable for $\langle (\delta p_{\mathrm{T}})^2 \rangle$, as medium effects are expected to reduce the momentum differences of non-flow particles as they are out of local equilibrium.

Extended Data Fig. 2 shows the N_{ch}-scaled values of $\langle v_2^2 \rangle$, $\langle (\delta p_{\mathrm{T}})^2 \rangle$ and $\langle v_2^2 \delta p_{\mathrm{T}} \rangle$ as a function of centrality in Au + Au collisions. The requirement of subevent reduces the signal in the most peripheral bin by 50%, 40% and 80%, respectively, which can be treated as the amount of non-flow rejected by the subevent requirement. Therefore, we use the differences between the standard and subevent methods to estimate the non-flow in the subevent method. These differences vary with centrality because of the combined effects of medium modification of non-flow and longitudinal flow decorrelations[77]. These differences are propagated to the ratios of these observables between U + U and Au + Au. They are found to be 1.1%, 3.5% and 11% for $R_{v_2^2}$, $R_{(\delta p_{\mathrm{T}})^2}$ and $R_{v_2^2 \delta p_{\mathrm{T}}}$, respectively.

Extended Data Fig. 2 also provides an estimate of non-flow based on the N_{ch}-scaling method. We assume that the entire signals in the 80–100% centrality in two-subevent are non-flow, and then use equation (10) to estimate the fraction of non-flow as a function of centrality. As mentioned earlier, we use this approach for $\langle v_2^2 \rangle$ and $\langle v_2^2 \delta p_{\mathrm{T}} \rangle$, in which the medium effects may redistribute non-flow correlations in azimuthal angle, instead of suppressing them. This approach is unsuitable for $\langle (\delta p_{\mathrm{T}})^2 \rangle$, for which the medium effects should always suppress the non-flow contribution. In the 0–5% most central collisions, the estimated non-flow is about 6% for $\langle v_2^2 \rangle$ and only about 1.4% for $\langle v_2^2 \delta p_{\mathrm{T}} \rangle$. These differences, when propagated to the ratios, are reduced for $R_{v_2^2}$, which is positive, and increased for $R_{v_2^2 \delta p_{\mathrm{T}}}$, which is negative. They amount to about 2.8% for $R_{v_2^2}$ and 2.5% for $R_{v_2^2 \delta p_{\mathrm{T}}}$.

The non-flow systematic uncertainties are taken as the larger of the two approaches for $R_{v_2^2}$ and $R_{v_2^2 \delta p_{\mathrm{T}}}$, whereas for $R_{(\delta p_{\mathrm{T}})^2}$, the difference between standard and subevent methods is used. The total non-flow uncertainties in the 0–5% centrality are 2.8%, 3.5% and 11% for $R_{v_2^2}$, $R_{(\delta p_{\mathrm{T}})^2}$ and $R_{v_2^2 \delta p_{\mathrm{T}}}$, respectively.

Extended Data Fig. 3 contrasts the non-flow systematic uncertainties with other sources of uncertainties (next section) in this analysis. In the 0–5% centrality, the non-flow uncertainties are comparable or slightly larger than other sources, whereas they are subdominant in other centrality ranges.

In the literature, non-flow contributions are sometimes estimated using the HIJING model[78], which has only non-flow correlations. The latter were found to follow very closely equation (10) (refs. 79,80). In our second approach, instead of relying on the HIJING model, we assume this N_{ch}-scaling behaviour but use real peripheral data as the baseline for non-flow contributions. Our findings indicate that the HIJING model fails to quantitatively capture the features of non-flow. Specifically, the HIJING model predicts a much weaker $\Delta\eta$ dependence for $\langle v_2^2\rangle$, with only a 13% difference between the standard and two-subevent methods, whereas the data indicate a 50% decrease[81] (fig. 25 in ref. 81 for $p+p$ collisions). Furthermore, we found that the values of $\langle v_2^2\delta p_T\rangle$ predicted by HIJING are three times larger than the data in peripheral Au + Au collisions. Therefore, the non-flow estimation based on the HIJING model in ref. 80 seems to be exaggerated. A more recent estimate[46], based on a transport model incorporating full medium dynamics and equation (10), yields a non-flow fraction consistent with STAR data. This study also suggests a potential increase of the $R_{v_2^2}$ with $\Delta\eta$ associated with flow decorrelation effects.

Understanding non-flow correlations as a physical process has always been a work in progress. As our knowledge deepens, the non-flow uncertainties are expected to reduce. Rather than merely contributing to experimental uncertainties or even being corrected for in the data, non-flow physics should ultimately be incorporated into hydrodynamic models. Currently, these models include non-flow effects from resonance decays but lack contributions from jet fragmentation.

Systematic uncertainties

Systematic uncertainties include an estimate of the non-flow contributions discussed above and other sources accounting for detector effects and analysis procedure. These other sources are estimated by varying the track quality selections, the z_{vtx} cuts, examining the influence of pileup, comparing results from periods with different detector conditions and closure test. The influence of track selection criteria is studied by varying the number of fit hits on the track from a minimum of 16 to 19 and by varying DCA cut from <3 cm to <2.5 cm, resulting in variations of 1–5% for $\langle(\delta p_T)^2\rangle$. The impacts on $\langle v_2^2\rangle$ and $\langle v_2^2\delta p_T\rangle$ are up to 2.5% and 4%, respectively.

The influence of track reconstruction on the collision vertex is examined by comparing the results for different $|z_{vtx}|$ cuts, with variations found to be 0.5–3% for all observables. Comparisons between data-taking periods, particularly normal and reverse magnetic field runs in Au + Au collisions, show consistency within their statistical uncertainties. The influence of pileup and background events is studied by varying the cut on the correlation between N_{ch}^{rec} and the number of hits in the TOF. The influence is found to be 1–3% for $\langle v_2^2\rangle$ and $\langle(\delta p_T)^2\rangle$, and reaches 2–10% for $\langle v_2^2\delta p_T\rangle$. Comparisons are also made between the 2010 and 2011 Au + Au datasets, which have different active acceptances in the TPC. The results are largely consistent with the quoted uncertainties, although some differences are observed, particularly in the central region, in which variations reach 5–10% for $\langle v_2^2\delta p_T\rangle$.

A closure test was conducted, in which the reconstruction efficiency and its variations in η and ϕ from the data were used to retain a fraction of the particles generated from a multi-phase transport model[82]. Subsequently, a track-by-track weight, as described in equation (9), was applied to the accepted particles. All observables are calculated using the accepted particles and compared with those obtained using the original particles. This procedure allowed us to recover $\langle v_2^2\rangle$ and $\langle(\delta p_T)^2\rangle$ within their statistical uncertainties. However, a 2–3% nonclosure was observed in $\langle v_2^2\delta p_T\rangle$. Nevertheless, it is important to note that such non-closures largely cancel when considering the ratios between U + U and Au + Au collisions.

Several additional cross-checks were carried out. The track reconstruction efficiency has about 5% uncertainty because of its reliance on particle type and occupancy dependence. We repeated the analysis by varying this efficiency, and the variations in the results were either less than 1% or consistent within their statistical uncertainties. The reconstructed p_T can differ from the true value because of finite momentum resolution. This effect was investigated by smearing the reconstructed p_T according to the known resolution, calculating the observable and comparing the results with the original ones. A discrepancy of approximately 0.5% was observed for $\langle(\delta p_T)^2\rangle$, whereas other observables remained consistent within their statistical uncertainties. These effects cancel in the ratios between °U + U and Au + Au collisions.

The default results are obtained from the two-subevent method. The total systematic uncertainties, including these sources and non-flow, are calculated as a function of centrality. The uncertainties of the ratios between U + U and Au + Au are evaluated for each source and combined in quadrature to form the total systematic uncertainties. This process results in a partial cancellation of the uncertainties between the two systems. The uncertainties from different sources discussed above on the ratios are shown by the black boxes in Extended Data Fig. 3. The total systematic uncertainties, including non-flow in the 0–5% centrality range, amount to 3.9%, 4.4% and 12.5% for $R_{v_2^2}$, $R_{(\delta p_T)^2}$, and $R_{v_2^2\delta p_T}$, respectively.

Hydrodynamic model setup and simulation

Extended Data Table 1 details the Woods–Saxon parameters for Au and U used in the IP-Glasma + MUSIC model calculations. The nucleon–nucleon inelastic cross-sections are the standard values 42 mb and 40.6 mb for Au + Au collisions at 200 GeV and U + U collisions at 193 GeV, respectively. For U, the nuclear shape in equation (1) is extended to include a possible small axial hexadecapole deformation β_4:

$$R(\theta,\phi) = R_0(1+\beta_2[\cos\gamma Y_{2,0} + \sin\gamma Y_{2,2}] + \beta_4 Y_{4,0}). \quad (11)$$

Most low-energy nuclear structure models favour a modest oblate deformation for ^{197}Au (ref. 34). We assume $\beta_{2Au} = 0.14$ and $\gamma_{Au} = 45°$ as the default choice for ^{197}Au, which are varied in the range of $\beta_{2Au} \approx 0.12$–0.14 and $\gamma_{Au} \approx 37$–$53°$ according to refs. 34,67. These calculations reasonably reproduce many observables related to the ground-state nuclear deformation. For ^{238}U, we scan several β_{2U} values ranging from 0 to 0.34. We also vary β_{4U} from 0 to 0.09 and γ_U in the range of 0°–20° to examine the sensitivity of the U + U results to hexadecapole deformation and triaxiality. For each setting, about 100,000–400,000 events are generated using the officially available IP-Glasma + MUSIC[25,44]. Each event is oversampled at least 100 times to minimize statistical fluctuations in the hadronic transport. These calculations were performed using services provided by the Open Science Grid Consortium[83,84].

The role of final state effects is studied by varying the shear and bulk viscosities simultaneously up and down by 50%. The impacts on $\langle v_2^2\rangle$, $\langle(\delta p_T)^2\rangle$ and $\langle v_2^2\delta p_T\rangle$ are shown for Au + Au collisions in Extended Data Fig. 4 (top). The values of these flow observables are changed by more than a factor of two as a function of centrality. Yet, the ratios between U + U and Au + Au collisions (Extended Data Fig. 4, bottom) are relatively stable. A small reduction of $R_{v_2^2}$ and $R_{(\delta p_T)^2}$ are observed in non-central collisions, when values of viscosities are halved. However, this change is an overestimate because the calculated flow observables greatly overestimate the data. So, in the end, half of the variations of the ratios are included in the model uncertainty.

The main theoretical uncertainties arise from variations in nuclear structure parameters. Parameters common between two collision systems, such as the minimum inter-nucleon distance in nuclei d_{min}, are not expected to contribute to the uncertainty significantly. However,

other parameters, including nuclear radius R_0, skin a and higher-order hexadecapole deformation β_4, could be different between Au and U and hence contribute more to the theoretical uncertainty.

Extended Data Table 1 provides a list of variations of nuclear structure parameters. The impact of these variations on ratios of flow observables is shown in Extended Data Fig. 5. The ratios of flow observables are insensitive to these variations in the most central collisions. $R_{v_2^2}$ is particularly sensitive to skin parameter a. This is understandable, as v_2 has a large contribution from the reaction plane flow, which varies strongly with the value of a (ref. 45).

Model uncertainties for the ratios are derived by combining the impact of varying viscosities, together with various sources from Extended Data Fig. 5. As a consequence, checks that are consistent with the default calculation within their statistical uncertainties do not contribute to the model uncertainties. The combined model uncertainties for 1 standard deviation are shown in Fig. 3.

A cross-check is conducted for an alternative hydrodynamic code, the Trajectum model[22,85]. This model has 20 parameter sets obtained from a Bayesian analysis of the Pb + Pb data at the LHC but was not tuned to the RHIC data. For this calculation, we simply repeat the calculation at RHIC energy and calculate the same observables. Although the description of $\langle v_2^2 \rangle$ and $\langle (\delta p_T)^2 \rangle$ is reasonable, several parameter sets give negative values of $\langle v_2^2 \delta p_T \rangle$ in mid-central collisions, and are subsequently not used. The calculation is performed for the remaining 16 parameter sets as a function of centrality, and root mean square variations among these calculations are assigned as the uncertainty.

Extended Data Fig. 6 shows the ratios of flow observables from Trajectum and compares them with IP-Glasma + MUSIC. The results from these two models agree in their uncertainties for $R_{v_2^2}$ and $R_{(\delta p_T)^2}$, with Trajectum predictions slightly higher in the UCC region. This leads to slightly lower values of β_{2U} than the IP-Glasma model: $\beta_{2U} = 0.228 \pm 0.013$ for $R_{v_2^2}$ and $\beta_{2U} = 0.276 \pm 0.018$ for $R_{(\delta p_T)^2}$.

For $R_{v_2^2 \delta p_T}$, however, the Trajectum model tends to systematically underpredict the data, as well as has much larger uncertainties compared with the IP-Glasma model. In central collisions, this discrepancy can be improved by using a larger triaxiality parameter value $\gamma_U \sim 15°$. Overall, the comparison of the Trajectum model with data gives similar constraints on β_{2U} with comparable uncertainties but a larger γ_U value with bigger uncertainties (next section).

Assigning uncertainties on β_{2U} and γ_U

A standard pseudo-experiment procedure, similar to that in ref. 86, is used to combine the uncertainties from $R_{(\delta p_T)^2}$ and $R_{v_2^2 \delta p_T}$ shown in Fig. 3g. We assume that the total uncertainties extracted from the two observables are independent, and we model the probability density function as follows:

$$P(\beta_{2U}, \gamma_U) \propto \exp\left(-\frac{(\beta_{2U} - \overline{\beta}_a)^2}{2\sigma_a^2} - \frac{(\beta_{2U} - \overline{\beta}_b(\gamma_U))^2}{2\sigma_b^2(\gamma_U)} \right). \quad (12)$$

Here, $\overline{\beta}_a = 0.294$ and $\sigma_a = 0.021$ represent the mean and uncertainty of β_{2U} extracted from $R_{(\delta p_T)^2}$ in Fig. 3g from the IP-Glasma + MUSIC model. Similarly, $\overline{\beta}_b$ and σ_b are the mean and uncertainty of β_{2U} from $R_{v_2^2 \delta p_T}$, and they depend on the parameter γ_U. We sample a uniform prior distribution in β_{2U} and γ_U to obtain the posterior distribution. From this posterior distribution, we obtained the mean and 1 standard deviation uncertainty of β_{2U} and γ_U, $\beta_{2U} = 0.297 \pm 0.015$ and $\gamma_U = 8.5° \pm 4.8°$, as well as the confidence contours shown in Fig. 3g. This statistical analysis is also performed for $R_{(\delta p_T)^2}$ and $R_{v_2^2 \delta p_T}$ for the Trajectum model, yielding constraints of $\beta_{2U} = 0.275 \pm 0.017$ and $\gamma_U = 15.5° \pm 7.8°$.

Finally, we perform an analysis to combine the constraints of the IP-Glasma + MUSIC and Trajectum models. This is achieved by multiplying the probability density function equation (12) from the two models, treating their constraints as statistically independent. This approach yields $\beta_{2U} = 0.286 \pm 0.012$ and $\gamma_U = 8.7° \pm 4.5°$. We noticed that the Trajectum model does not affect the constraints on γ_U because of the large uncertainty of the model, but the uncertainty on β_{2U} reduces markedly because of the comparable precision in the two models. Therefore, we also include the difference of the extracted β_{2U} values between the two models as an additional theoretical uncertainty. The final constraints given by this procedure are $\beta_{2U} = 0.286 \pm 0.025$ and $\gamma_U = 8.7° \pm 4.5°$.

Data availability

All raw data for this study were collected using the STAR detector at Brookhaven National Laboratory and are not available to the public. Derived data supporting the findings of this study are publicly available in the HEPData repository (https://www.hepdata.net/record/147196) or from the corresponding author on request.

Code availability

The codes to process raw data collected by the STAR detector are publicly available on GitHub (https://github.com/star-bnl). The codes to analyse the produced data are not publicly available.

53. Giacalone, G., Guerrero-Rodríguez, P., Luzum, M., Marquet, C. & Ollitrault, J.-Y. Fluctuations in heavy-ion collisions generated by QCD interactions in the color glass condensate effective theory. *Phys. Rev. C* **100**, 024905 (2019).
54. Giacalone, G. Many-body correlations for nuclear physics across scales: from nuclei to quark-gluon plasmas to hadron distributions. *Eur. Phys. J. A* **59**, 297 (2023).
55. Li, B.-A. Uranium on uranium collisions at relativistic energies. *Phys. Rev. C* **61**, 021903 (2000).
56. Shuryak, E. V. High energy collisions of strongly deformed nuclei: an old idea with a new twist. *Phys. Rev. C* **61**, 034905 (2000).
57. Filip, P., Lednicky, R., Masui, H. & Xu, N. Initial eccentricity in deformed ^{197}Au+^{197}Au and ^{238}U+^{238}U collisions at $\sqrt{s_{NN}}$=200 GeV at the BNL Relativistic Heavy Ion Collider. *Phys. Rev. C* **80**, 054903 (2009).
58. Shou, Q. Y. et al. Parameterization of deformed nuclei for Glauber modeling in relativistic heavy ion collisions. *Phys. Lett. B* **749**, 215–220 (2015).
59. Goldschmidt, A., Qiu, Z., Shen, C. & Heinz, U. Collision geometry and flow in uranium + uranium collisions. *Phys. Rev. C* **92**, 044903 (2015).
60. STAR Collaboration.Azimuthal anisotropy in U+U and Au+Au collisions at RHIC. *Phys. Rev. Lett.* **115**, 222301 (2015).
61. ALICE Collaboration. Anisotropic flow in Xe–Xe collisions at $\sqrt{s_{NN}}$=5.44 TeV. *Phys. Lett. B* **784**, 82–95 (2018).
62. CMS Collaboration. Charged-particle angular correlations in XeXe collisions at $\sqrt{s_{NN}}$=5.44 TeV. *Phys. Rev. C* **100**, 044902 (2019).
63. ATLAS Collaboration. Measurement of the azimuthal anisotropy of charged-particle production in Xe+Xe collisions at $\sqrt{s_{NN}}$=5.44 TeV with the ATLAS detector. *Phys. Rev. C* **101**, 024906 (2020).
64. Giacalone, G., Noronha-Hostler, J., Luzum, M. & Ollitrault, J.-Y. Hydrodynamic predictions for 5.44 TeV Xe+Xe collisions. *Phys. Rev. C* **97**, 034904 (2018).
65. Giacalone, G. Constraining the quadrupole deformation of atomic nuclei with relativistic nuclear collisions. *Phys. Rev. C* **102**, 024901 (2020).
66. Giacalone, G., Jia, J. & Zhang, C. Impact of nuclear deformation on relativistic heavy-ion collisions: assessing consistency in nuclear physics across energy scales. *Phys. Rev. Lett.* **127**, 242301 (2021).
67. Ryssens, W., Giacalone, G., Schenke, B. & Shen, C. Evidence of hexadecapole deformation in uranium-238 at the relativistic heavy ion collider. *Phys. Rev. Lett.* **130**, 212302 (2023).
68. Robledo, L. M., Rodriguez-Guzmán, R. R. & Sarriguren, P. Evolution of nuclear shapes in medium mass isotopes from a microscopic perspective. *Phys. Rev. C* **78**, 034314 (2008).
69. Bally, B., Bender, M., Giacalone, G. & Somà, V. Evidence of the triaxial structure of ^{129}Xe at the Large Hadron Collider. *Phys. Rev. Lett.* **128**, 082301 (2022).
70. Bally, B., Giacalone, G. & Bender, M. Structure of ^{128,129,130}Xe through multi-reference energy density functional calculations. *Eur. Phys. J. A* **58**, 187 (2022).
71. Fortier, N., Jeon, S. & Gale, C. Comparisons and predictions for collisions of deformed ^{238}U nuclei at $\sqrt{s_{NN}}$=193 GeV. Preprint at https://arxiv.org/abs/2308.09816 (2023).
72. Bieser, F. S. et al. The STAR trigger. *Nucl. Instrum. Methods Phys. Res. A* **499**, 766–777 (2003).
73. Liope, W. J. Multigap RPCs in the STAR experiment at RHIC. *Nucl. Instrum. Methods Phys. Res. A* **661**, S110–S113 (2012).
74. Adamczyk, L. et al. Measurements of dielectron production in Au+Au collisions at $\sqrt{s_{NN}}$=200 GeV from the STAR Experiment. *Phys. Rev. C* **92**, 024912 (2015).
75. Jia, J., Zhou, M. & Trzupek, A. Revealing long-range multiparticle collectivity in small collision systems via subevent cumulants. *Phys. Rev. C* **96**, 034906 (2017).
76. Borghini, N., Dinh, P. M. & Ollitrault, J.-Y. A new method for measuring azimuthal distributions in nucleus-nucleus collisions. *Phys. Rev. C* **63**, 054906 (2001).
77. Aad, G. et al. Longitudinal flow decorrelations in Xe+Xe collisions at $\sqrt{s_{NN}}$=5.44 TeV with the ATLAS Detector. *Phys. Rev. Lett.* **126**, 122301 (2021).
78. Gyulassy, M. & Wang, X.-N. HIJING 1.0: a Monte Carlo program for parton and particle production in high energy hadronic and nuclear collisions. *Comput. Phys. Commun.* **83**, 307–331 (1994).

79. Bhatta, S., Zhang, C. & Jia, J. Higher-order transverse momentum fluctuations in heavy-ion collisions. *Phys. Rev. C* **105**, 024904 (2022).
80. Wang, F. The nonflow issue in connecting anisotropy measurements to hydrodynamics in relativistic heavy-ion collisions. Preprint at arxiv.org/abs/2402.03222 (2024).
81. STAR Collaboration. Measurement of flow coefficients in high-multiplicity p+Au, d+Au and ^{3}He+Au collisions at $\sqrt{s_{NN}}$=200 GeV. Preprint at https://arxiv.org/abs/2312.07464 (2023).
82. Lin, Z.-W., Ko, C. M., Li, B.-A., Zhang, B. & Pal, S. Multiphase transport model for relativistic heavy ion collisions. *Phys. Rev. C* **72**, 064901 (2005).
83. Pordes, R. et al. The open science grid. *J. Phys. Conf. Ser.* **78**, 012057 (2007).
84. Sfiligoi, I. et al. The pilot way to grid resources using glideinWMS. In *2009 WRI World Congress on Computer Science and Information Engineering*, Vol. 2, 428–432 (IEEE, 2009).
85. Nijs, G. & van der Schee, W. A generalized hydrodynamizing initial stage for heavy ion collisions. Preprint at arxiv.org/abs/2304.06191 (2023).
86. Nisius, R. On the combination of correlated estimates of a physics observable. *Eur. Phys. J. C* **74**, 3004 (2014).

Acknowledgements We thank the RHIC Operations Group and RCF at BNL, the NERSC Center at LBNL and the Open Science Grid consortium for providing resources and support. This work was supported in part by the Office of Nuclear Physics in the US DOE Office of Science, the US National Science Foundation, National Natural Science Foundation of China, Chinese Academy of Sciences, the Ministry of Science and Technology of China and the Chinese Ministry of Education, the Higher Education Sprout Project by Ministry of Education at NCKU, the National Research Foundation of Korea, Czech Science Foundation and Ministry of Education, Youth and Sports of the Czech Republic, Hungarian National Research, Development and Innovation Office, New National Excellency Programme of the Hungarian Ministry of Human Capacities, the Department of Atomic Energy and Department of Science and Technology of the Government of India, the National Science Centre and WUT ID-UB of Poland, the Ministry of Science, Education and Sports of the Republic of Croatia, German Bundesministerium für Bildung, Wissenschaft, Forschung and Technologie (BMBF), Helmholtz Association, the Ministry of Education, Culture, Sports, Science, and Technology (MEXT), the Japan Society for the Promotion of Science (JSPS) and the Agencia Nacional de Investigación y Desarrollo (ANID) of Chile. We thank C. Shen for providing the IP-Glasma+MUSIC code and G. Nijs for providing the Trajectum code. We thank G. Giacalone, D. Lee, T. Rodriguez, B. Schenke, H. Song and Y. Zhou for their discussions and comments.

Author contributions All authors contributed to all research steps and writing of the paper.

Competing interests The authors declare no competing interests.

Additional information
Correspondence and requests for materials should be addressed to the STAR Collaboration.
Peer review information *Nature* thanks the anonymous reviewers for their contribution to the peer review of this work.

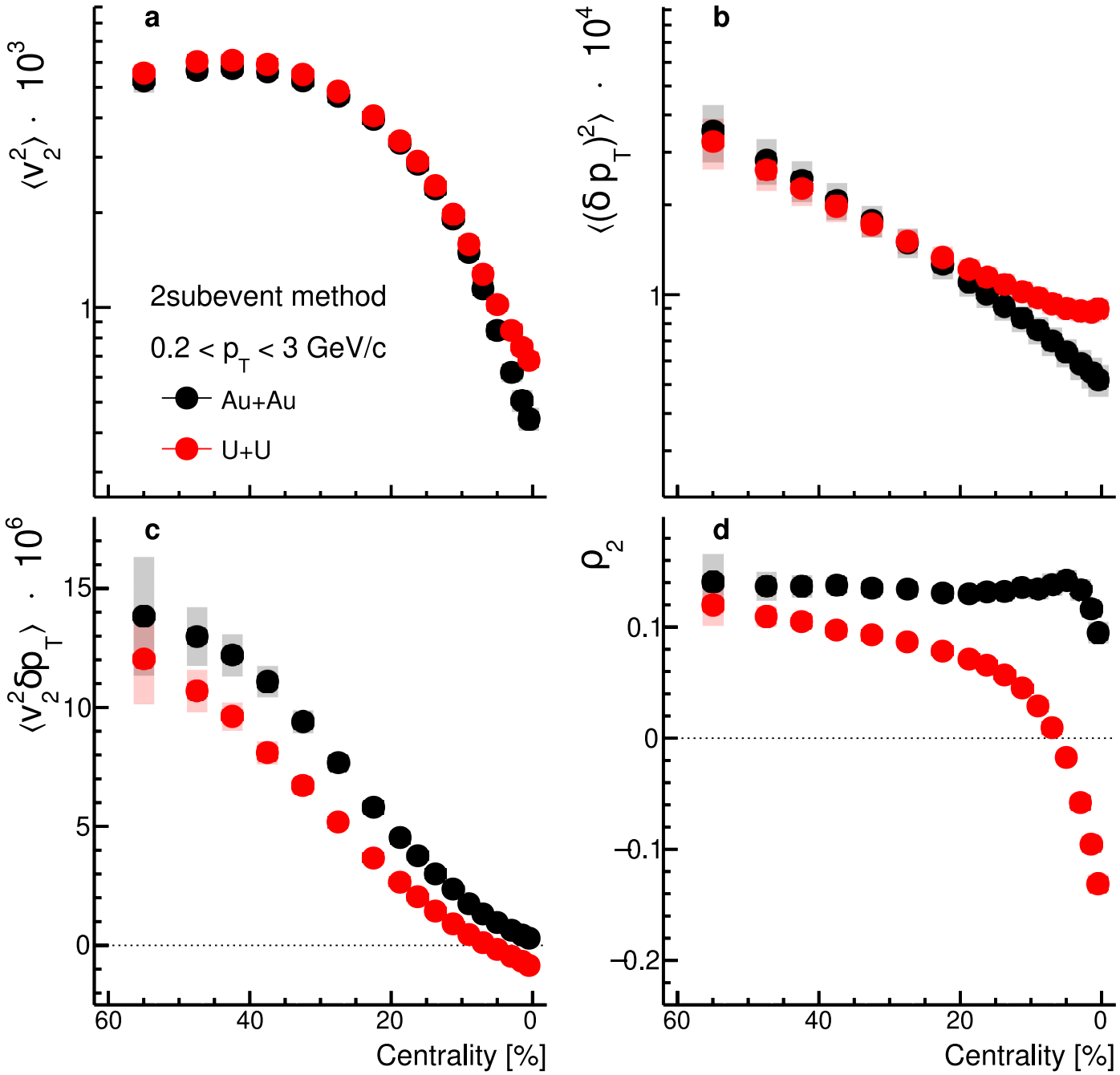

Extended Data Fig. 1 | Components involved in v_2-[p_T] correlations. The centrality dependences of $\langle v_2^2 \rangle$ (**a**), $\langle (\delta p_T)^2 \rangle$ (**b**), $\langle v_2^2 \delta p_T \rangle$ (**c**) and $\rho_2 = \langle v_2^2 \delta p_T \rangle / (\langle v_2^2 \rangle \sqrt{\langle (\delta p_T)^2 \rangle})$ (**d**) in U+U (red) and Au+Au (black) collisions. They are calculated using the two-subevent method. The error bars and shaded bands are statistical and systematic uncertainties, respectively.

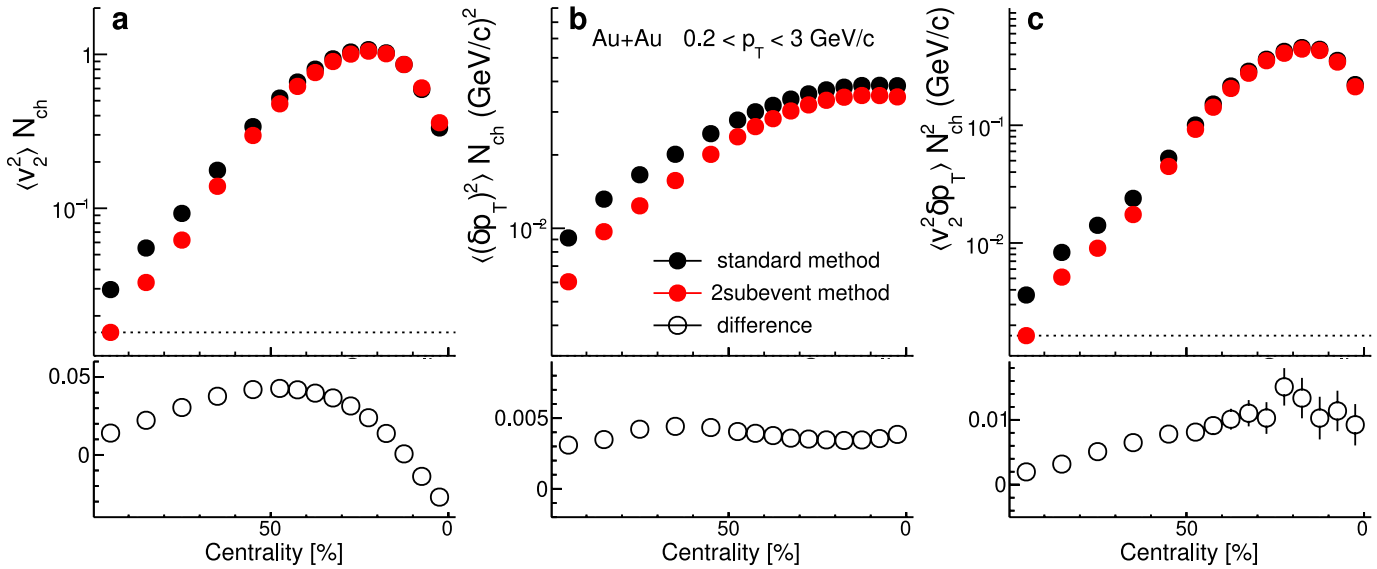

Extended Data Fig. 2 | Impact of non-flow correlations. The centrality dependence of N_{ch} scaled quantities in Au+Au collisions, $\langle v_2^2 \rangle N_{ch}$ (**a**), $\langle (\delta p_T)^2 \rangle N_{ch}$ (**b**), and $\langle v_2^2 \delta p_T \rangle N_{ch}^2$ (**c**) from the standard method (black solid markers), two-subevent method (red solid markers) and their differences (open markers). The error bars are statistical uncertainties. The decrease of $\langle v_2^2 \rangle$-difference towards central collisions is attributed to two-track reconstruction effects in the standard method, which does not affect the other two observables. The dashed lines indicate the upper limit of the non-flow contribution, assuming N_{ch}-scaling of Eq. (10).

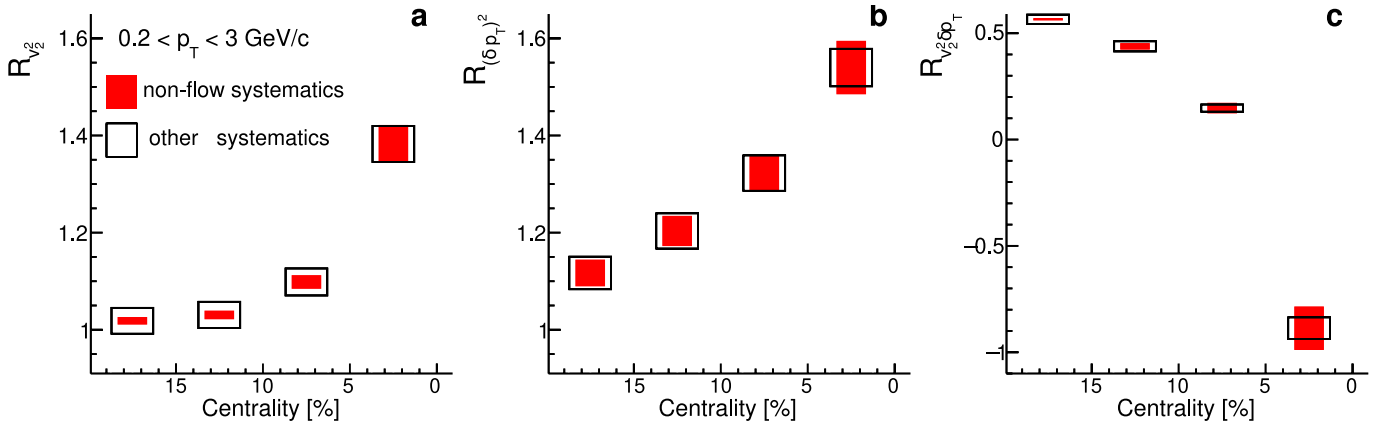

Extended Data Fig. 3 | Summary of the systematic uncertainties. The centrality dependence of ratios $R_{v_2^2}$ (a), $R_{(\delta p_T)^2}$ (b), and $R_{v_2^2\delta p_T}$ (c) from the two-subevent method with the systematic uncertainties arising from the non-flow estimate (red bars) and other sources (black boxes).

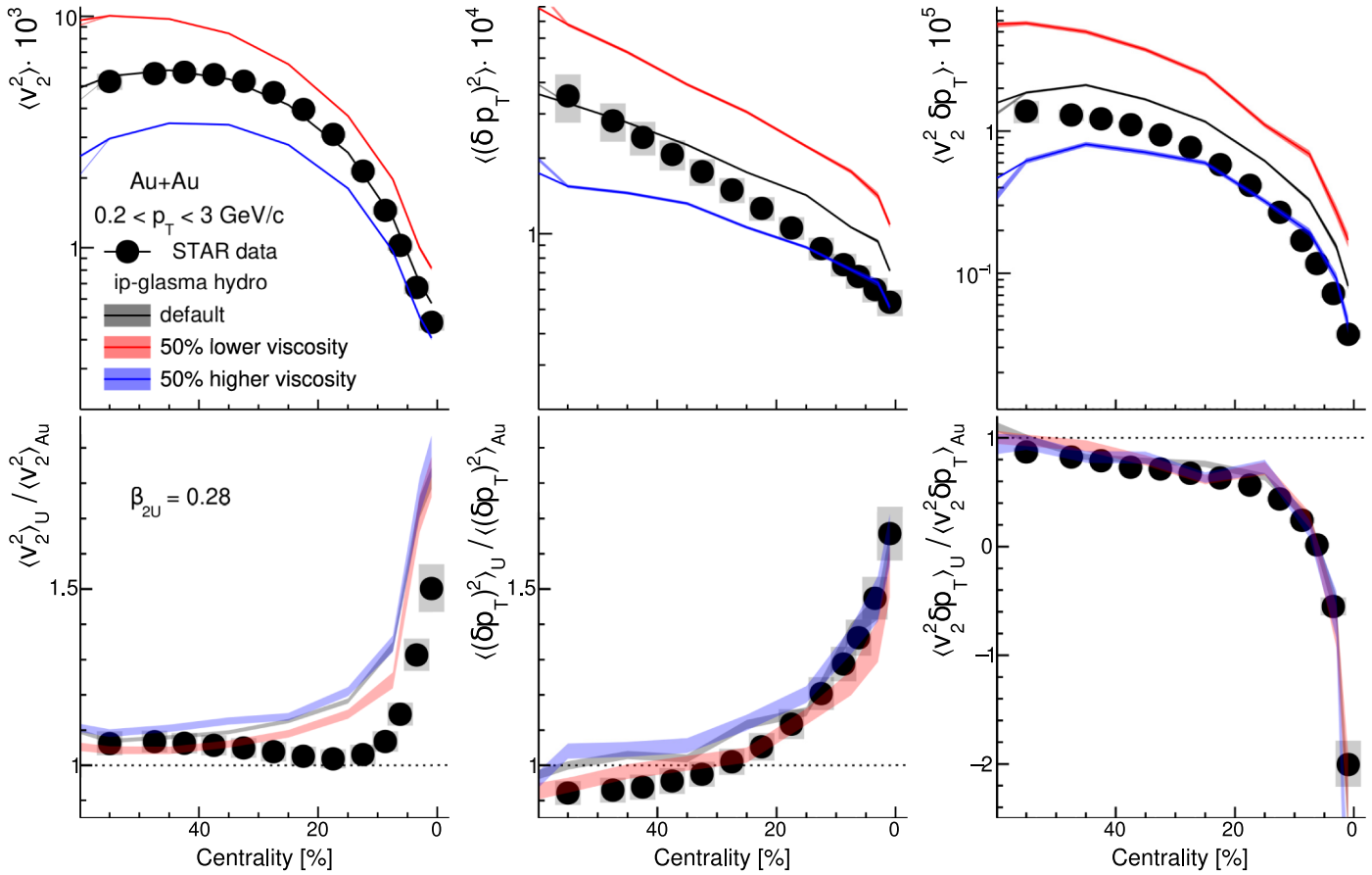

Extended Data Fig. 4 | Sensitivity to shear and bulk viscosities of the QGP. IP-Glasma+MUSIC model prediction of the $\langle v_2^2 \rangle$ (left), $\langle (\delta p_T)^2 \rangle$ (middle) and $\langle v_2^2 \delta p_T \rangle$ (right) compared with the data in Au+Au collisions and the corresponding ratios (bottom) between U+U and Au+Au collisions, for different amount of shear and bulk viscosities.

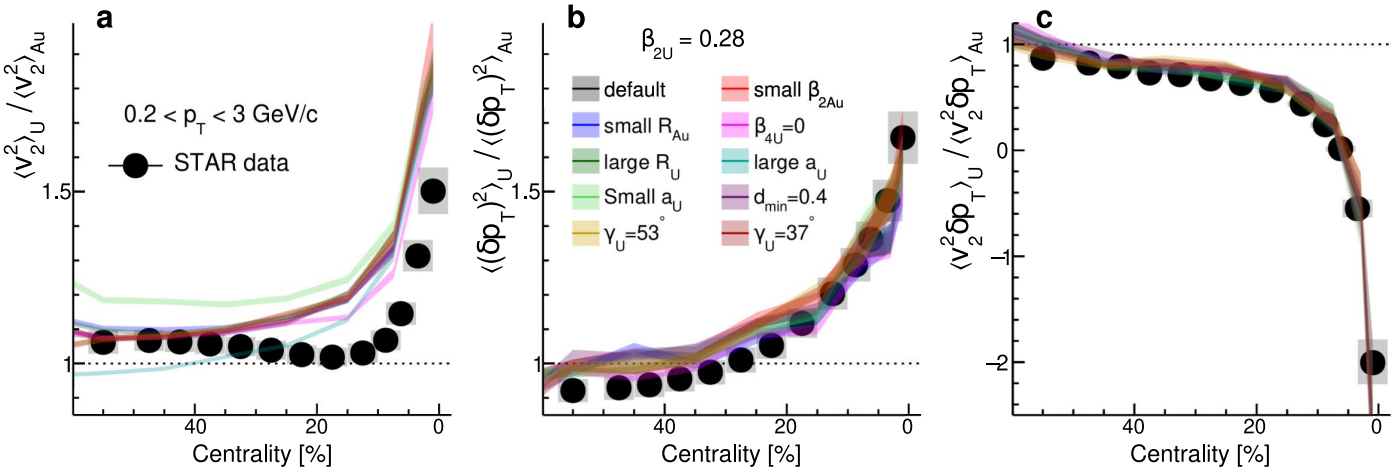

Extended Data Fig. 5 | Sensitivity to nuclear structure parameters. IP-Glasma+MUSIC model prediction of the ratios of $\langle v_2^2\rangle$ (**a**), $\langle (\delta p_T)^2\rangle$ (**b**), and $\langle v_2^2 \delta p_T\rangle$ (**c**) between U+U and Au+Au collisions. The calculations are done for different Glauber model parameters, and they are compared with the data.

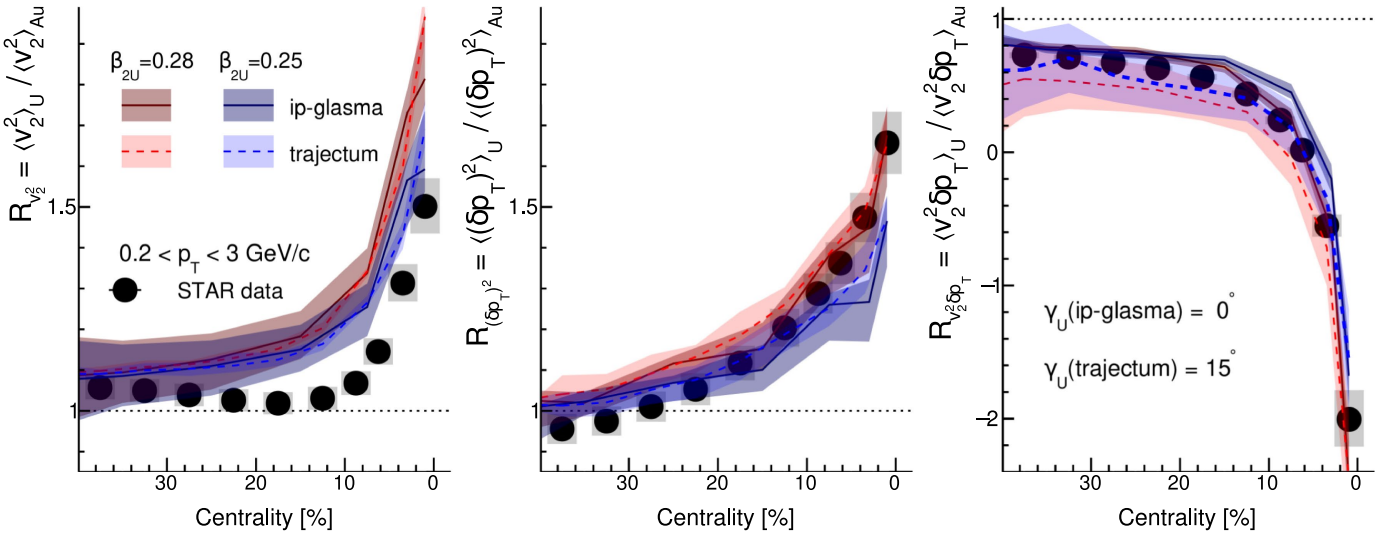

Extended Data Fig. 6 | Comparison between two hydrodynamic models. The ratios of $\langle v_2^2 \rangle$ (left), $\langle (\delta p_T)^2 \rangle$ (middle) and $\langle v_2^2 \delta p_T \rangle$ (right) as a function of centrality from IP-Glasma+MUSIC (solid lines) and Trajectum (dashed lines), assuming $\beta_{2U} = 0.28$ (red) and $\beta_{2U} = 0.25$ (blue). For the IP-Glasma+MUSIC model, only the uncertainties for the default configuration are shown for clarity. They are compared to the data.

Extended Data Table 1 | Choices of Woods-Saxon parameters in the IP-Glasma+MUSIC model

Species	R(fm)	a (fm)	$d_{\min}$(fm)	β_2	β_4	γ (°)
^{197}Au	**6.62**,6.38	**0.52**	**0.9**, 0.4	**0.14**,0.12	**0**	53, **45**, 37
^{238}U	**6.81**,7.07	**0.55** 0.495 0.605	**0.9**, 0.4	0,0.15 0.22, 0.25 **0.28**,0.34	**0.09**,0	**0**, 10 15, 20

The default values are denoted by bold font. At the same time, the rest are variations designed to constrain the values of (β_{2U}, γ_U) and derive theoretical uncertainties associated with other structure parameters.